2015

Gravity Constraints on the Geometry of the Big Bend of the San Andreas Fault in the Southern Carrizo Plains and Pine Mountain Region

Ali Can Altintas

FLORIDA STATE UNIVERSITY

COLLEGE OF ARTS AND SCIENCES

GRAVITY CONSTRAINTS ON THE GEOMETRY OF THE BIG BEND OF THE SAN ANDREAS FAULT IN THE SOUTHERN CARRIZO PLAINS AND PINE MOUNTAIN REGION

By

ALI CAN ALTINTAS

A Thesis submitted to the
Department of Earth, Ocean, and Atmospheric Science
in partial fulfillment of the
requirements for the degree of
Master of Science

2015

Ali Can Altintas defended this thesis on November 9, 2015.
The members of the supervisory committee were:

David W. Farris
Professor Directing Thesis

James F. Tull
Committee Member

Stephen Kish
Committee Member

The Graduate School has verified and approved the above-named committee members, and certifies that the thesis has been approved in accordance with university requirements.

ACKNOWLEDGMENTS

I have to say that it has been a great two and half year for me in Tallahassee. This city and university taught me a lot more than I thought before I came here. First of all, I would like to thank a lot to my advisor Dr. David Farris. His mentorship and guidance helped me a lot to get my Master's degree. I would not be the geologist I am today, if it were not for him. Also I want to thank to my committee members Dr. James Tull and Dr. Stephen Kish. They did their best to guide me and I learned a lot from them. Special thanks to Dr. Neil Lundberg, Dr. Yang Wang and Dr. William Parker for being great teachers. I am so grateful for my graduate student friends/colleagues in my department. Since the first day I have felt like I am at home because of them.

TABLE OF CONTENTS

LIST OF FIGURES

ABSTRACT

The goal of this project is to combine gravity measurements with geologic observations to better understand the "Big Bend" of the San Andreas Fault (SAF) and its role in producing hydrocarbon-bearing structures in the southern Central Valley of California. The SAF is the main plate boundary structure between the Pacific and North American plates and accommodates ≈35 mm/yr of dextral motion. The SAF can be divided into three main parts: the northern, central and southern segments. The boundary between the central and southern segments is the "Big Bend", which is characterized by an ≈30°, eastward bend. This fault curvature led to the creation of a series of roughly east-west thrust faults and the transverse mountain ranges.

Four high-resolution gravity transects were conducted across locations on either side of the bend. A total of 166 new gravity measurements were collected. Previous studies suggest significantly inclined dip angle for the San Andreas Fault in the Big Bend area. Yet, our models indicate that the San Andreas Fault is near vertical in the Big Bend area. Also gravity cross-section models suggest that flower structures occur on either side of the bend. These structures are dominated by sedimentary rocks in the north and igneous rocks in the south. The two northern transects in the Carrizo plains have an ≈-70 mgal Bouguer anomaly. The SAF has a strike of ≈315° near these transects. The northern transects are characterized by multiple fault strands which cut marine and terrestrial Miocene sedimentary rocks as well as Quaternary alluvial valley deposits. These fault strands are characterized by ≈6 mgal short wavelength variations in the Bouguer gravity anomaly, which correspond to low density fault gouge and fault splays that juxtapose rocks of varying densities. The southern transects cross part of the SAF with a strike of 285°, have a Bouguer anomaly of ≈-50 mgal and are characterized by a broad 15 mgal high. At this location

the rocks on either side of the fault are Proterozoic - Cretaceous metamorphic or/and plutonic rocks. Previous work based on geologic mapping hypothesized the existence of a shallow, low angle Abel Mountain Thrust in which crystalline rocks were thrust over Miocene sedimentary rocks, near Apache Saddle. However, gravity models indicate the crystalline rocks are vertically extensive and form a positive flower structure bounded by high angle faults. Also, based on the thickness of fault adjacent sedimentary cover, the gravity models suggest a minimum exhumation of 5-6 km for crystalline rocks in the south. Assuming exhumation began with the switch from the transtensional San Gabriel Fault to transpressional San Andreas Fault at approximately 5 Ma, this indicates exhumation rates of 1 km/Ma. Overall, the broad gravity highs observed along the southern transects are due to uplift of basement rocks in this area.

CHAPTER 1

INTRODUCTION

The San Andreas Fault system is defined as a network of mostly right lateral strike-slip faults that accommodate approximately two-thirds of the motion between the North American and the Pacific plates. Geodetic estimates suggest that this system accommodates 35 mm/yr of slip out of total 50 mm/yr in the boundary between the North American and the Pacific plates (Wallace, 1990). This, almost 1300 km long, great transform fault system is the dominant geologic structure on a very important plate boundary. In the north, the San Andreas Fault system ends at the Mendocino triple junction, which is the point the Gorda, North American and Pacific plates meet. In the south, the San Andreas Fault system terminates at incipient spreading centers in the Salton Sea that extend southward into the Gulf of California (Figure 1.1). The San Andreas Fault is the primary plate boundary but also there are other important branches and faults in this system. (e.g. Hayward and Calaveras faults in central California and San Jacinto and Elsinore faults in southern California.) There are also many smaller branches in this system but most of them are considered extensions of bigger faults. For example, Rodgers Creek and Maacama faults in northern California are usually treated as northward extensions of the Hayward fault. In general, the San Andreas Fault can be divided into three main segments: the northern, central and southern segments. The central segment has a relatively simple geometry with the San Andreas Fault itself being the main fault. Also the creeping section of the San Andreas Fault lies in this segment. To the north and south this situation changes dramatically. The northern segment is characterized by multiple right lateral strike-slip faults in addition to the San Andreas Fault. In the southern segment, south of Bakersfield, the main San Andreas Fault curves to the east, and is commonly

referred as the Big Bend. This curvature exhibits an approximately 30 degrees eastward bend in the fault and seperates the central and southern segments. In addition, the Big Bend caused led to the creation of a series of roughly east-west thrust faults (e.g. Sierra Madre fault) and the Transverse mountain ranges. South of this location this plate boundary is defined once again by multiple parallel strike-slip faults.

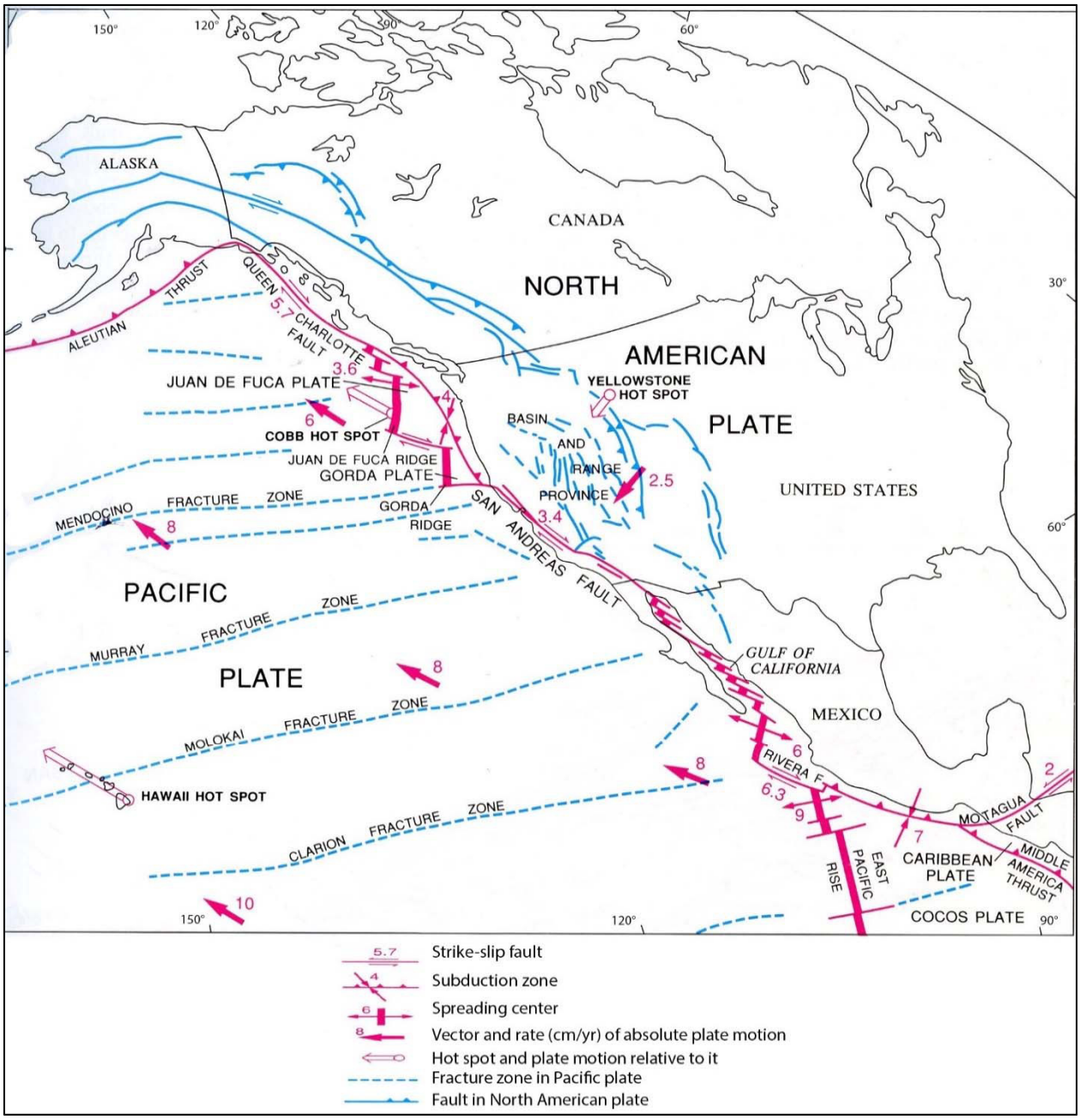

Figure 1.1. Northeast Pacific Basin (modified from USGS Professional Paper 1515).

1.1. Plate Tectonic Development of the San Andreas Fault

Plate tectonics is a theory that explains the large scale motion of the Earth's lithosphere. This theory is a modern version of Alfred Wegener's continental drift theory. At the time Wegener could not come up with reasonable explanations for how continents move around the planet. Due to lack of evidence Wegener's theory was not generally accepted. However, at the beginning of the 1960's, Hess and Deitz described a "sea-floor spreading" theory that provided a mechanism for how continents move. Plate tectonics theory is a blend of these two theories. According to plate tectonics theory, the Earth's surface is covered by series of rigid lithospheric plates and tectonic activity occurs along their margins. Oceanic crust is continuously generated at and is moving away from spreading centers, whereas at subduction zones lithospheric plates sink into the mantle and are destroyed. Ultimately, mantle convection drives the movement of plates, and the heat. Source that drives the convection is the radioactivity deep in the Earth's mantle.

Most tectonic movement occurs at plate boundaries. There are three different kind of plate boundaries which are divergent, convergent and transform boundaries. Divergent boundaries develop along spreading centers. At spreading centers, plates are moving apart from each other and new oceanic crust is created by upwelling of magma from the mantle. Plates that are moving towards each other exhibit convergent plate boundaries. Plates can be destroyed (or recycled) in the subduction zones or can collide with each other and create mountain ranges in the collisional convergent plate boundaries. There are three different types of convergence. In oceanic-continental convergence, more dense oceanic crust subducts under the continental crust and this process creates a volcanic arc. In oceanic-oceanic convergence, two oceanic plates converge one is usually subducts under the other and this process creates an island arc. In continental-continental convergence, two different continental plate converge towards each other and neither of them

subducted because continental rocks are not dense enough to sink. So these two continental plates collide and this process creates huge mountain ranges like Himalayas. Transform boundaries are places where lithospheric plates slide past each other. At transform boundaries, there is no creation or destruction of lithosphere.

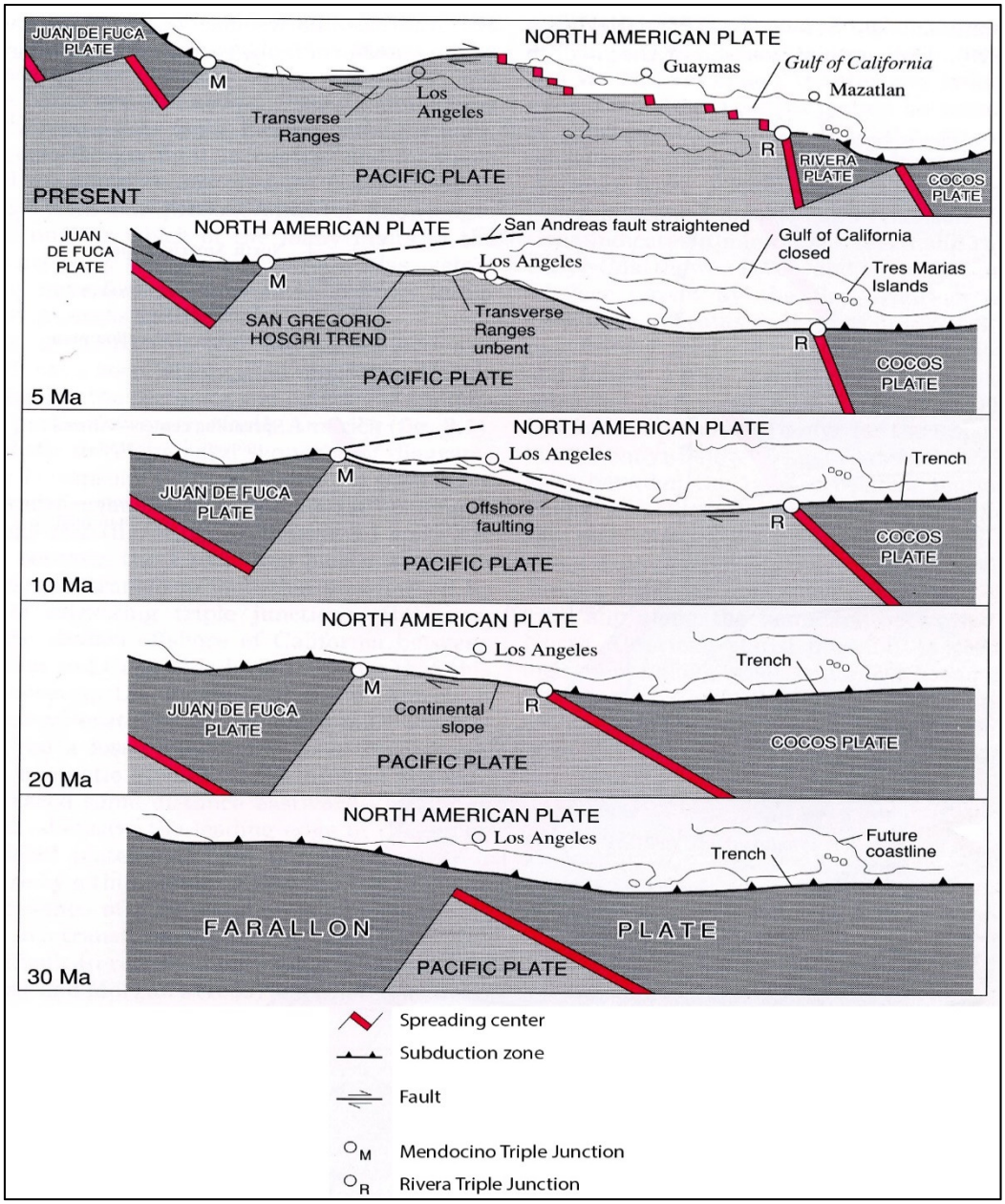

Figure 1.2. Diagrams show plate tectonic evolution of the San Andreas Fault (modified from USGS Professional Paper 1515).

The western coast of North America is an active tectonic zone with continental North

American crust to the east, and oceanic Pacific crust to the west. In the north, relative movement between these two plates is convergent, and the Juan de Fuca plate subducts beneath North America. Yet, most of the relative motion in this area is right lateral with the Pacific plate moving in a northwest direction relative to North America. As two plates slide past one another, crustal slices or fragments are carried to distant locations. Such crustal fragments are known as terranes, and they juxtaposed against each other rocks of potentially very different lithology, age, stratigraphy, and metamorphism. The existence of numerous blueschist and ophiolite belts along the western coast of North America (Irwin, 1977) shows that some of the terranes are associated with subduction during Paleozoic and Mesozoic time. The Mesozoic margin of California exhibits a classic subduction sequence with a preserved accretionary prism (Franciscan mélange), forearc basin (Great Valley sequence), and arc batholith (the Sierra Nevada batholith).

However, the details of Mesozoic and earlier tectonic margin, previous to the development of the San Andreas Fault, are still debated. Some geologists (Dickinson, 1981) state that there was a convergent plate interaction in this area to create Andean-like continental margin. Whereas others observe paleontologic and paleomagnetic data and suggest that some Late Mesozoic rocks of Coast Ranges were carried north from places close to Equator previous to accretion to North America and deposition of Great Valley sequence (Hopson and others, 1986). In this model, the Franciscan mélange, parts of Coast Range ophiolite and overlying Great Valley sequence moved to north as far as 1120 km due to another dextral translation in Late Cretaceous and early Tertiary time (McLaughlin and others, 1988).

Magnetic anomaly patterns in oceanic crust are the main source to understand the rates and directions of relative motions between tectonic plates. The patterns show convergent plate motion relative to North America during early Tertiary time due to the subduction of the Farallon plate.

Formation of the San Andreas Fault system began no earlier than about 30 Ma (late Oligocene), when the East Pacific rise first encroached on the North American plate (McKenzie and Morgan, 1969; Atwater, 1970). Triple junctions originated at locations where the Pacific plate impinged upon the North America and then moved to northwest and southeast as subduction of Farallon plate carried on. The two triple junctions, Mendocino and Rivera triple junctions, are now 2500 km away from each other. The transform fault growth accommodated the relative motion in this elongating boundary between the Pacific and North American plates and this relative motion was dextral. Early transform motion was not on the modern trace of the San Andreas Fault (Figure 1.2). However, there are several ancestral strike-slip faults now preserved in the Transverse and Coast Ranges of California (e.g. the San Gabriel Fault). The modern San Andreas Fault did not appear in southern California until the opening of the Gulf of California during Pliocene time, at about 4 Ma. Since that time Baja California has migrated 260 km away from mainland Mexico (Larson and others, 1968). The San Andreas Fault is the boundary between the Pacific and North American plates; yet there is something unique in this zone. Rocks on the west side of the San Andreas Fault are now moving with the Pacific plate but these rocks are initially formed as part of the North American plate.

As early development of the San Andreas Fault system continued, the main movement must have been on an initial transform fault between the Pacific and North American plates as the triple junction moved to the south and north at the respective ends of the fault. During this triple junction movement the transform clearly jumped eastward into the North American plate one or more times and to became the northern section of the modern San Andreas Fault. The modern trace of the fault in central California most likely had only minor slip until about 12.5-10 Ma and was not the dominant strand before 7.5-5 Ma (Dickinson and Snyder, 1979). Similar eastward

transform fault jumps also created the southern section of the San Andreas Fault and caused the opening of the Gulf of California. Some of the major faults that are between the San Andreas Fault and continental margin might symbolize ancient locations of the transform. Some those faults are still active. Viable candidates for such ancient faults are the San Gregorio-Hosgri fault in central and northern California and the San Gabriel, Elsinore or offshore faults in southern California.

The present rate of relative motion between Pacific and North American plates has been estimated at about 6 cm/yr (Atwater, 1970) to 5.6 cm/yr (Minster and Jordan, 1978). This rate possibly has varied over time (Atwater and Molnar, 1973). Yet, it is obvious that the relative motion between the two plates is greater than the amount accommodated by the San Andreas Fault. The difference between the rate of relative plate motion on the Pacific and North American plate boundary and the rate of slip on the San Andreas Fault has been observed by many geologists (Atwater, 1970; Minster and Jordan, 1978; Weldon and Humphreys, 1986). Recent geodetically constrained estimates of slip on the San Andreas Fault indicate rates of 30-35 mm/yr. Other faults in a broad zone extending throughout the North American Cordillera accommodate the rest of the total slip along the plate boundary. That broad zone stretches from the Pacific margin to the east as far as Rio Grande Rift.

1.2. Geologic Settings

The San Andreas Fault separates main crustal structures all along California (Figure 1.3). We can basically divide this crustal structures as the ones in Northern and Central California, and the ones in Southern California. In northern and central California, the fault is surrounded by Salinian block of granitic and metamorphic rocks on the west and the Franciscan mélange and the Great Valley sequence on the east. In southern California, the fault cut the basement rocks which are generally Precambrian and younger metamorphic and plutonic rocks.

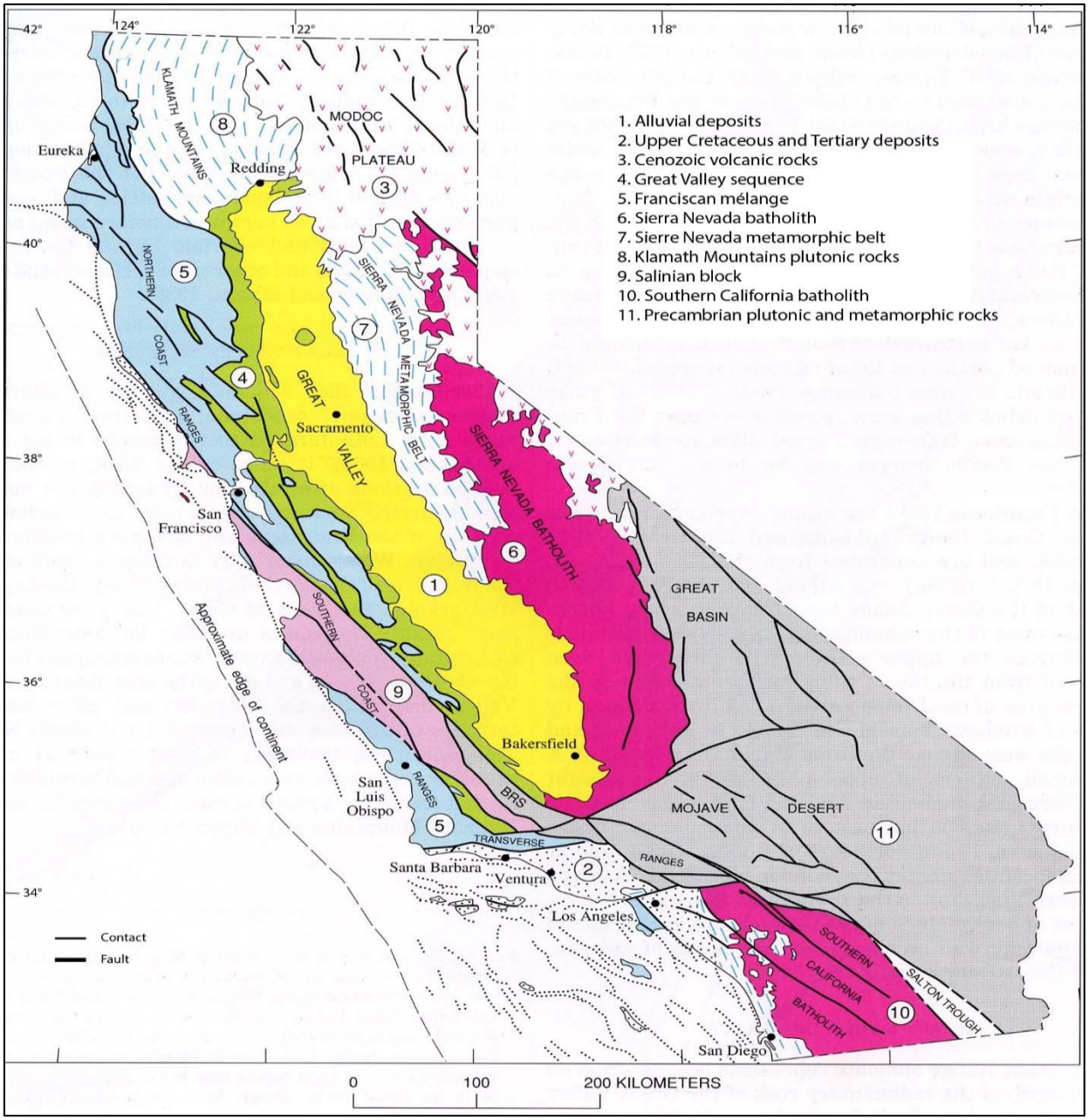

Figure 1.3. Geology of California (modified from USGS Professional Paper 1515).

1.2.1. Northern and Central California

1.2.1.1. Franciscan Rocks

Along the Coast Ranges in northern and central California, Franciscan rocks appear east of the San Andreas Fault. However, at certain locations Franciscan rocks are overlain by the Coast Range ophiolite and the Great Valley sequence, and are separated from them by the Coast Range

thrust (Bailey and others, 1970). The Franciscan mélange consists of highly sheared greywacke, shale, and lesser amounts of mafic volcanic rocks, thin-bedded chert, and limestone. Presence of foraminifers in limestones and radiolarians in the chert indicates a marine origin for the Franciscan mélange. These rocks are mainly Late Jurassic and Cretaceous in age (Bailey and others, 1964), yet some of the chert and volcanic rocks are as old as Early Jurassic (Irwin and others, 1977; Blome and Irwin, 1983).

1.2.1.2. Coast Range Ophiolite

The Coast Range ophiolite is a fragment of oceanic crust that the sedimentary Great Valley sequence rocks have been deposited on. From base to the top; a general ophiolite sequence consists of peridotite, layered gabbro, massive gabbro, dikes and volcanic rocks (pillow lavas). However, only in certain places is the complete lithologic sequence of the Coast Range ophiolite exposed because the Coast Range ophiolite is remarkably sheared, thinned and in many places it is missing due to faulting. In locations that expose a complete sequence of the Coast Range ophiolite, its thickness varies from 3 km to 5 km (Hopson and others, 1981).

1.2.1.3. Great Valley Sequence

The Great Valley sequence is composed of interbedded mudstone, sandstone and conglomerate that range from Late Jurassic to Cretaceous age (Bailey and others, 1964). It has more lateral continuity than the Franciscan sedimentary rocks. Also it appears as thick, regularly bedded sections of strata. Along the western side of northern Great Valley, this sequence is completely developed and it has a thickness up to 12 km. If uninterrupted by faults, this sequence sits above the Coast Range ophiolite. In addition, the Great valley sequence overlies older basement terranes of the Klamath Mountains and Sierra Nevada on the east side of the Great Valley.

1.2.1.4. Salinian Block

From the Transverse Ranges to Bodega Head, rocks of the Salinian block are present almost all along the west wall of the San Andreas Fault. The Salinian block are comprised of western, northern, and central belts, and also generally the Barrett Ridge slice is included in the Salinian block. However, basement rocks of the Barrett Ridge slice are more likely a northward continuation of San Gabriel Mountain rocks due to similar metamorphic and granitic lithologies, and a schist similar to the Pelona schist (Ross, 1984). Granitic and metamorphic rocks are main formations of these western, central and northern belts. Upper Cretaceous and younger strata overlie these granitic and metamorphic rocks. Moderate to high-grade gneiss, granofels, impure quartzite, and minor schist and marble are some of the metamorphic rocks in this area, and these rocks have protoliths of thinly bedded siltstone and sandstone (Ross, 1978). The metamorphic rocks of the central and northern belts have a lower metamorphic grade than the western belt. Granite and tonalite are the most abundant plutonic rocks in this area. Yet, the plutonic rocks can range in composition to gabbro. The plutonic activity started at approximately 120-105 Ma in the northwestern part of the Salinian block according to U-Pb isotopic dating studies on zircon, and ended at approximately 80-75 Ma.

Some scientists debate if the Salinian block was a part of the Sierra Nevada batholith or if it is a far traveled terrane. (King, 1959; Page, 1981). However, Ross (1984) stated that there are too significant lithologic and geochronologic similarities between the Sierra Nevada batholith and the Salinian terrane. In contrast, paleomagnetic data suggests that the Salinian block may have moved from 2500 km south to present position since the Cretaceous (Champion and others, 1984) in which case it would have been generated near the latitude of Central America (Page, 1982). However, most workers conclude that the Salinian block is part of the same Mesozoic Cordilleran

batholith as the Sierra Nevada.

1.2.2. Southern California

The Big Bend in the San Andreas Fault is the boundary between southern part of Sierra Nevada batholith and the Transverse Ranges. South of the bend, the fault moves southeast along the northern San Gabriel Mountains and the edge of the Mojave Desert for almost 100 km. Continuing southward, the fault cuts between the San Gabriel and San Bernardino Mountains near the intersection of the San Jacinto fault. Mesozoic plutons and their Precambrian metamorphic and plutonic host rocks are the main rock units traversed by the San Andreas Fault in the Transverse Ranges.

Bedrock adjacent to the fault is overlain by the Quaternary deposits of Salton Trough for a length of almost 200 km south of Transverse Ranges. To the southeast, the Salton Trough widens and there are multiple strike-slip faults in this area. The Salton Trough region exhibits significant tectonic complexity. The San Andreas Fault forms the east wall of Salton Trough. Precambrian rocks and Mesozoic plutons and schist are abundant east of trough. These plutons and schist are similar to rocks in the Orocopia and Chocolate Mountains (Figure 1.4). Cretaceous plutonic rocks of the Southern California batholith and their metamorphic host rocks form the western wall of the Salton Trough. These rocks are similar to those in the San Jacinto Mountains. The Salton Trough, in contrast to basement blocks on either side, is filled with Quaternary and older Cenozoic sedimentary rocks (Fuis and others, 1982). The width of sedimentary fill is smaller (approximately 20 km) north of the Salton Trough and increases up to 60 km wide at the United States-Mexico border. The Salton Trough is also the location of spreading centers into which the southern San Andreas Fault terminates.

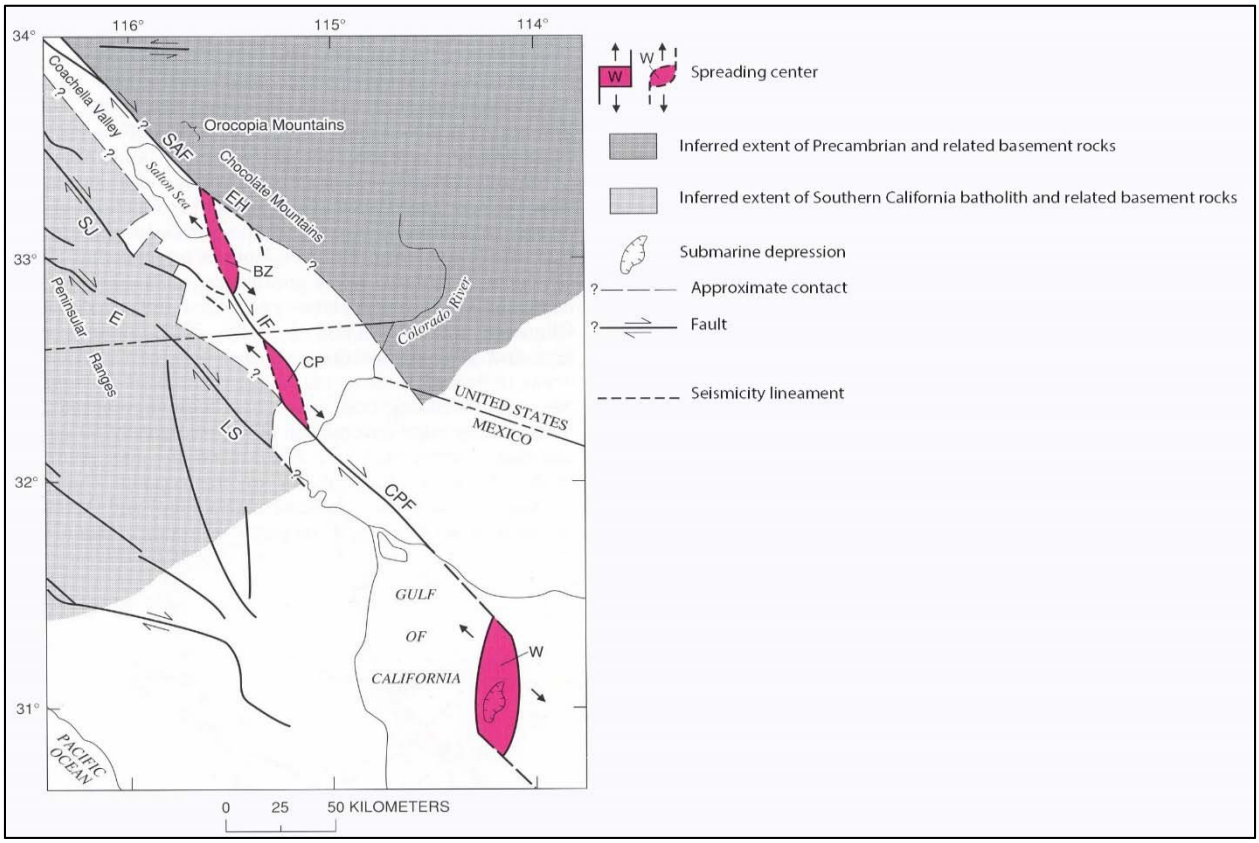

Figure 1.4. Salton Trough and northern Gulf of California (modified from USGS Professional Paper 1515).

The San Andreas Fault cuts Precambrian rocks and Mesozoic plutons which create most of the crystalline basement in the southern California. Those rocks can be observed sit above younger underthrust metamorphic rocks (e.g. the Catalina, Pelona, Rand and Orocopia schist units). The Catalina, Pelona, Rand and Orocopia schists and other similar units are generally interpreted as blueschist rocks correlative with the Franciscan, but were underthrust beneath the arc during the Late Cretaceous and Early Tertiary. Southwest of the San Andreas Fault, rocks are divided into two plates by the Vincent thrust in the San Gabriel Mountains. Ehlig (1981) stated that the Precambrian gneiss-amphibolite-granite complex (U-Pb age approx. 1700 Ma; Silver, 1966) forms the upper plate of this thrust and that complex is intruded by a Precambrian anorthosite-syenite-gabbro complex (U-Pb age=1220 Ma; Silver, 1971), all of which are intruded by the Late Triassic Lowe Granodiorite (U-Pb age=220 Ma; Silver, 1971), by mid-Mesozoic

rhyolitic to basaltic dikes, and finally, by granitic plutons of probable Late Cretaceous age (U-Pb age=80 Ma; Carter and Silver, 1971). The oldest rocks in the upper plate are probable remains of a Precambrian craton. In the Mojave Desert and San Bernardino Mountains, lower Paleozoic miogeoclinal strata overlies some Precambrian rocks on the northeast of the fault (Burchfield and Davis, 1981; Ehlig, 1981).

The Pelona Schist forms the lower plate of the Vincent thrust. Pelona Schist is mostly a sedimentary section of arkosic sandstone, siltstone, and shale which has been metamorphosed to white mica-quartz-albite schist and regionally have metavolcanic rokcs, metachert, marble, and serpentinite (Ehlig, 1981). San Gabriel Mountains have an uncovered section of Pelona Schist with a thickness of 3.5 km. Sedimentary structures are well conserved in the lowest 1 km of the section due to the decrease in metamorphic grade downward, away from the fault. This situation suggests that the metamorphism of the lower plate rocks occurred during thrusting. Pelona-type schist also can be seen under the Precambrian rocks of the Barrett Ridge slice and exposed in some points along the Garlock fault. Pelona-type schist and the Vincent-Orocopia thrust outcrops continue to the southwestern Arizona (Haxel and Dillon, 1978).

1.3. Regional Geology

1.3.1. Northern Transects and Vicinity

Four high-resolution gravity transects were conducted across locations on either side of the Big Bend of the San Andreas Fault. Two of them were on the northern side of the bend (Elkhorn Hills) and close to Maricopa, CA and the southern part of the Carrizo Plain. The Elkhorn Hills, which are an uplifted platform, are located in the southeastern Carrizo Plain. They bound the San Andreas Fault on the southwest and exhibit fault propagation folds on the northeast (Arrowsmith, 1995). Numerous extensional grabens and half-grabens, whose geometry correspond with

extension and San Andreas Fault related dextral shear, are situated in the center of Elkhorn Hills (Arrowsmith, 1995; Arrowsmith et al., 1998). The Plio-Quaternary Paso Robles Formation is the primary geologic unit that crops out in the Elkhorn Hills. This Paso Robles Formation is comprised of clay, silt, sand and gravel that is originated from the Miocene rocks of the Temblor Range to the northeast. The formation contains Pink, Tan and Gray members on the southwest side of the San Andreas Fault (Arrowsmith, 1995). The mid-Late Tertiary Santa Margarita and Bitterwater Creek Formations are overlain by the Paso Robles Formation. The mid-Late Tertiary Santa Margarita Formation consists of sandstones and conglomerates, whereas the Bitterwater Creek Formation is composed of gray marine mudstone and siltstone. An alluvial unit, which is comprised of channel and debris flow deposits, overlies all these formations. This alluvial unit may be coeval with the deposition of the Gray member of the Paso Robles Formation (Wallace, 1973).

The San Andreas Fault is characterized by a topographic feature known as Elkhorn Scarp along its northeastern margin. This topographic feature formed by lateral offset along the San Andreas Fault and small component of vertical surface uplift. The Paso Robles Formation also crops out in the area due to uplift along this boundary. The same uplift also juxtaposes the Paso Robles Formation with the old Pleistocene Temblor rangefront. Near the northeast of Elkhorn Hills, shortening caused by a blind reverse fault separates uplifted and exposed Paso Robles Formation from the old alluvial fan. This alluvial fan surface might symbolize the active Pleistocene Temblor rangefront.

Furthermore, numerous grabens and half-grabens, which lie parallel to the San Andreas Fault, occur in the hanging-wall of the thrust accounted for the uplift of the Elkhorn Hills. The right-stepping, en echelon geometry of the grabens show that a component of the San Andreas

Fault parallel shear influences their predominantly normal motion (Arrowsmith, 1995). The extensional grabens in the hanging-wall of the Elkhorn Hills thrust suggest that total deformation expanded from northwest to southeast, similar to the shortening deformation in the area.

The presence of both normal and reverse faulting in the Elkhorn Hills is probably caused by a down-dip steepening of the thrust fault geometry which is also responsible for uplift of the Elkhorn Hills (Arrowsmith, 1995). So a steep reverse fault near the location of the San Andreas Fault results in the curvature of a hanging-wall sheet. This process causes extension above the change in fault geometry. Dextral motion along the San Andreas Fault is transferred to the thrust sheet and determines a component of shear on the normal faults created in the hanging-wall. It also illustrates that local extension with a dextral shear component may originate in a transpressive environment (Arrowsmith, 1995).

The structural geology of this part of the Carrizo Plain indicates continuous contraction along the San Andreas Fault from northwest to southeast. Pressure ridges provide relatively small amounts of transpression on the north of the Elkhorn Hills. A rising amplitude of folding and relative offset of the Pleistocene Temblor rangefront within the hills suggests that deformation along the hill boundaries expands continuously from northwest to the southeast in the area. Also continuous extension in the Elkhorn Hills grabens suggests that increasing slip along the blind reverse faults accounted for uplift of the Elkhorn Hills towards the southeast. Such continuous deformation agrees with the counter-clockwise rotation of the San Andreas Fault as it enters the Big Bend in southern California. In addition, increasing deformation in locations near to faults in the Elkhorn Hills show a connection between deformation and the evolution of the restraining bend of the San Andreas Fault in southern California (Arrowsmith, 1995).

1.3.2. Southern Transects and Vicinity

The southern transects for gravity survey were cross part of the San Andreas Fault with an azimuth strike of 285 deg. The fault at this location is at an approximate 30 deg. angle to the Pacific – North America plate motion and is within the transverse ranges (the San Emigdio Mountains) thought to be created by Big Bend related thrust faults. Gravity was measured on the both sides of the San Andreas Fault in these transects. The rocks on the north side of the San Andreas Fault are crystalline basement rocks. These basement rocks comprised of four east to northeast trending belts of rock which are a northernmost gabbro and amphibolite belt, a tonalitic and amphibolitic gneiss belt, a window of Rand schist, and a granitic belt. Upper Triassic to Jurassic calc-silicate hornfels and marbles can be seen in tonalitic and granitic sequences. Upper plate rock belts overlie the Rand schist along the late Cretaceous to pre-Eocene Pastoria thrust. These upper plate rock belts are connected to Sierra Nevada batholith. A thick sequence of Eocene to upper Miocene marine strata, which dips toward the San Joaquin Valley, overlie the crystalline rocks along the northern San Emigdio Mountains. Miocene to Pleistocene lacustrine and alluvial deposits overlie the marine sedimentary sequence.

South of the San Andreas Fault, crystalline rocks of the Mount Pinos-Abel Mountain massif, which is comprised of Precambrian and Mesozoic metamorphic and plutonic (mostly granitic) rocks, and Pelona schist. These metamorphic and plutonic rocks are uninterrupted in the subsurface and extended as far as northern Carrizo Plains. These rocks are known as the Barrett Ridge Slice (Ross 1977). A thick sequence of Tertiary strata overlie the crystalline rocks on the south of the San Andreas Fault. These Tertiary strata have significant component of non-marine rocks, whereas the contemporaneous marine-dominated section occurs north of the fault.

CHAPTER 2

FIELD WORK AND DATA PROCESSING

2.1. Methodology

A gravimeter measures variations in the strength of the Earth's gravitational field. Gravity prospecting locates local masses of higher or lower density than the surrounding rock units and places constraints on their geometry and composition from the irregularities in the Earth's field. It is impossible to identify a unique source based on observed gravity anomalies alone. However, if geologic or other geophysical constraints exist, gravity observations can help distinguish between competing hypotheses through the use of quantitative modeling.

Gravity prospecting is a relatively inexpensive but a useful tool for geologic exploration. Gravity data can also be used in seismic interpretation to constrain results. For mineral exploration, gravity prospecting is generally a secondary method, and it is used for detailed follow-up of magnetic and electromagnetic anomalies during base metal surveys. Gravity surveys are also used in engineering and archeological studies.

Local differences in the densities of rocks near the surface cause changes in the gravity field. Often gravity and magnetic methods are used together as potential field techniques but there are fundamental differences between them. Gravity is a natural property of mass while magnetism state of a matter depends different factors such as the inducing fields and the orientations of magnetic domains. Density changes are relatively small and the effects of local masses' gravity are minute compared to the effect of background field of the Earth, but magnetic anomalies usually depend the combined effect of induced and remnant field component. The Earth's magnetic field

has complex changes with the time, whereas gravity is near constant if Earth tides are ignored. Overall, gravity anomalies depend mainly on density variations in subsurface rocks once appropriate corrections have been applied, whereas magnetic anomalies can be more difficult to interpret.

2.2. Field Work

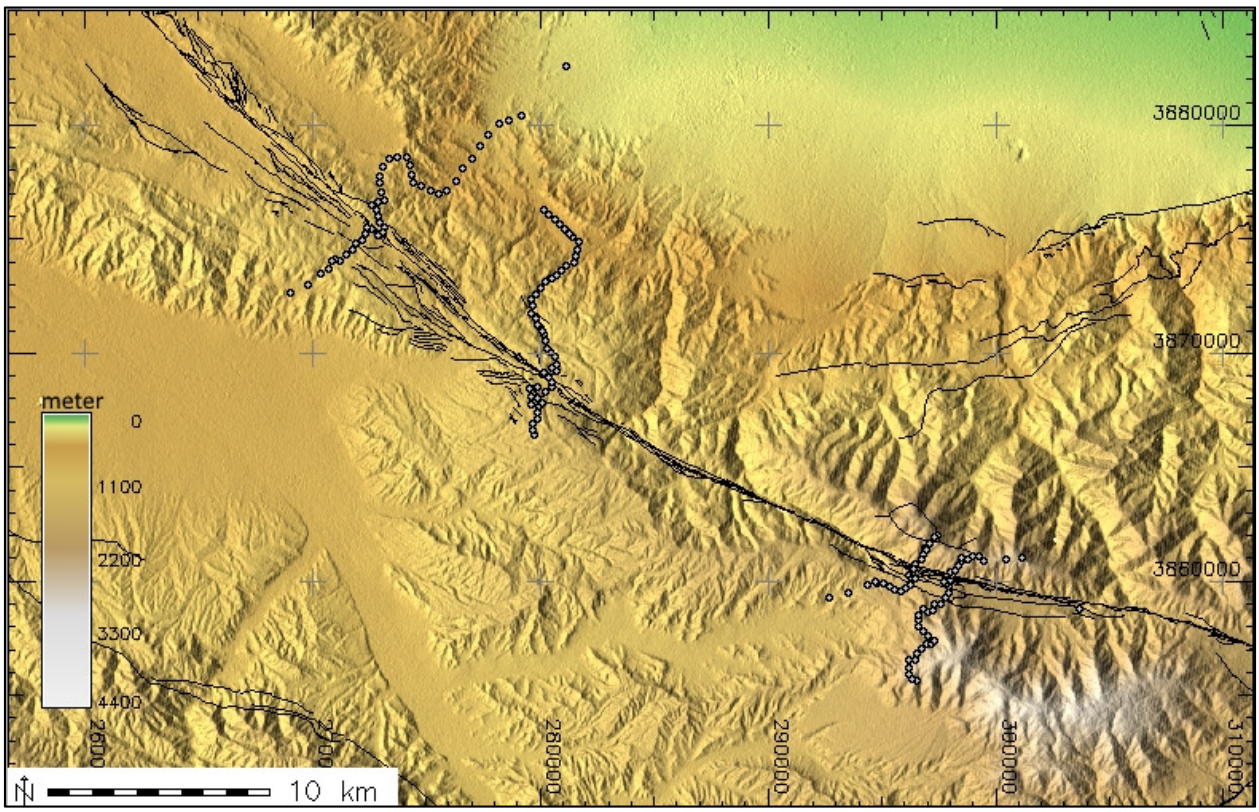

Figure 2.1. Topography map of the field work area. (Stations are shown as circles.)

This gravity survey described here was conducted using a Worden gravimeter and took place in the Big Bend region of the San Andreas Fault. The goal of the project is better define the geometry of the bend and its overall tectonic influence near its inflection point. To this end four high-resolution gravity transects were conducted across locations on either side of the bend. The northern transects were near Maricopa, CA and the southern end of the Carrizo plain. The SAF has an azimuth strike of approximately 315 deg. at this transect. There are productive oil fields

just east of the San Andreas Fault at this location, and the bend in the fault may be involved in the creation of hydrocarbon bearing structural traps. The southern transects were across part of the SAF with an azimuth strike of 285 deg. The fault at this location is at an approximate 30 deg. angle to the Pacific – North America plate motion and is within the transverse ranges thought to be created by Big Bend related thrust faults.

The gravity measurements were gathered in 166 stations with an average spacing of 0.3 kilometers. Station locations and elevations were measured with a Trimble Pro XRT differential GPS receiver and tied to absolute values using base station data from the National Geodetic Survey. Most stations have a horizontal and elevation accuracy less than 10 cm. Gravity survey points in the area are shown on a regional topographic and regional Bouguer gravity anomaly maps (Figure 2.1 and 2.2).

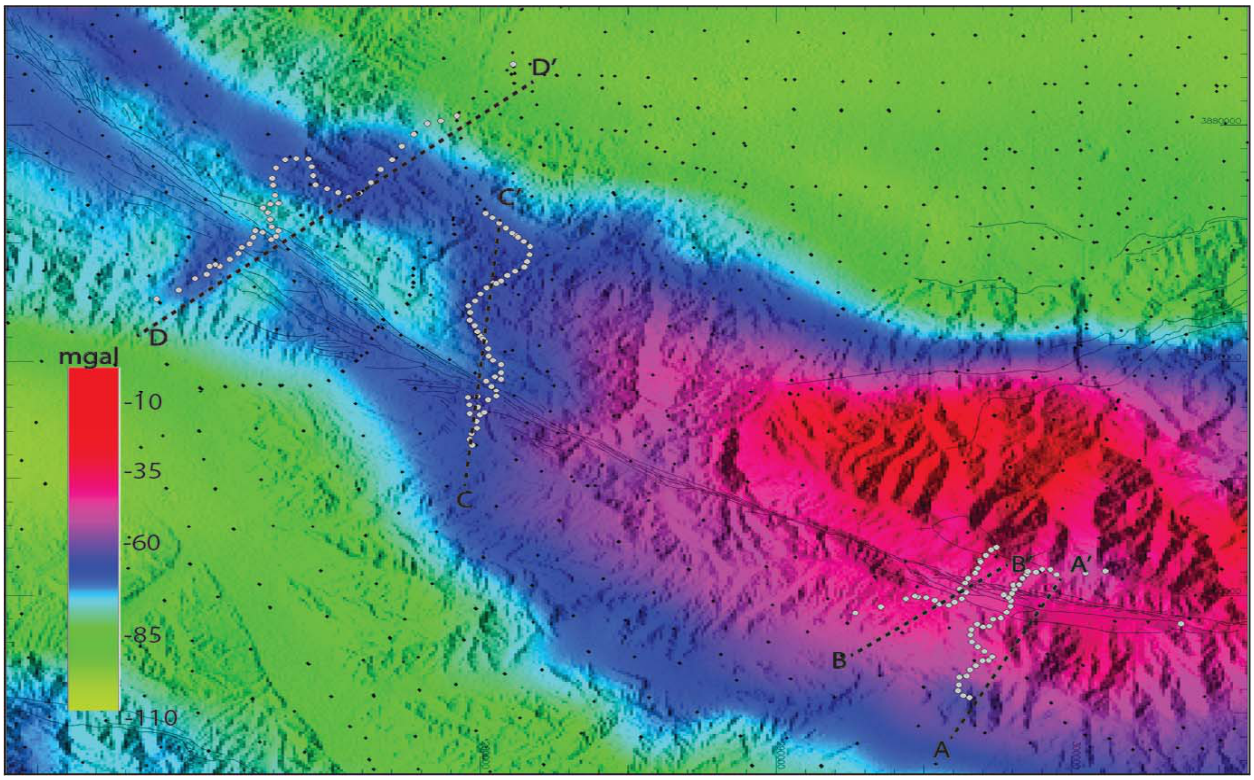

Figure 2.2. Bouguer gravity anomaly map of the field work area. (Stations are shown as circles. Dashed lines represent structural model profiles.)

2.3. Data Processing

2.3.1. Free-Air Correction

This correction makes up for height of the gravity station above sea-level or the specified vertical datum, and are applied after corrections for latitude. Latitude corrections were done using the WGS84 international gravity reference formula. Elevations in this project are measured with respect to the EGM96 geoid. The increase in height indicates an increase in distance from Earth's center of mass. An average value of 0.3086 mgal for every meter above sea surface was used. The calculated value after applying the free-air correction is known as free-air anomaly.

2.3.2. Simple Bouguer Correction

Topographic masses are located irregularly so an accurate calculation of their effects is difficult and approximation is necessary. The simplest method presumes that topography can be approximated by a flat plate, with constant density and thickness equal to the height of the gravity station above the reference surface, extending infinitely to all directions. This is known as the simple Bouguer correction. For the standard 2.67 gr/cm^3 density, the simple Bouguer correction is 0.1119 mgal/m. The calculated value after applying simple Bouguer correction is known as the simple Bouguer anomaly.

2.3.3. Interpolated Terrain Correction

In high relief areas (e.g. mountains or valleys), a more detailed topographic correction is needed to interpret the underlying geology. When simple Bouguer correction is inadequate, terrain correction is also used. For example if a topographic mass (mountain) above the gravity station applies an upward pull in gravity meter, its effect is negative and the correction is positive. However, a valley beyond the gravity station fills a place that simple Bouguer correction assumed to be occupied with rock that would apply a downward gravitational pull. Actually that rock is not

there. Terrain correction makes up for overcorrection by the simple Bouguer correction and is again positive.

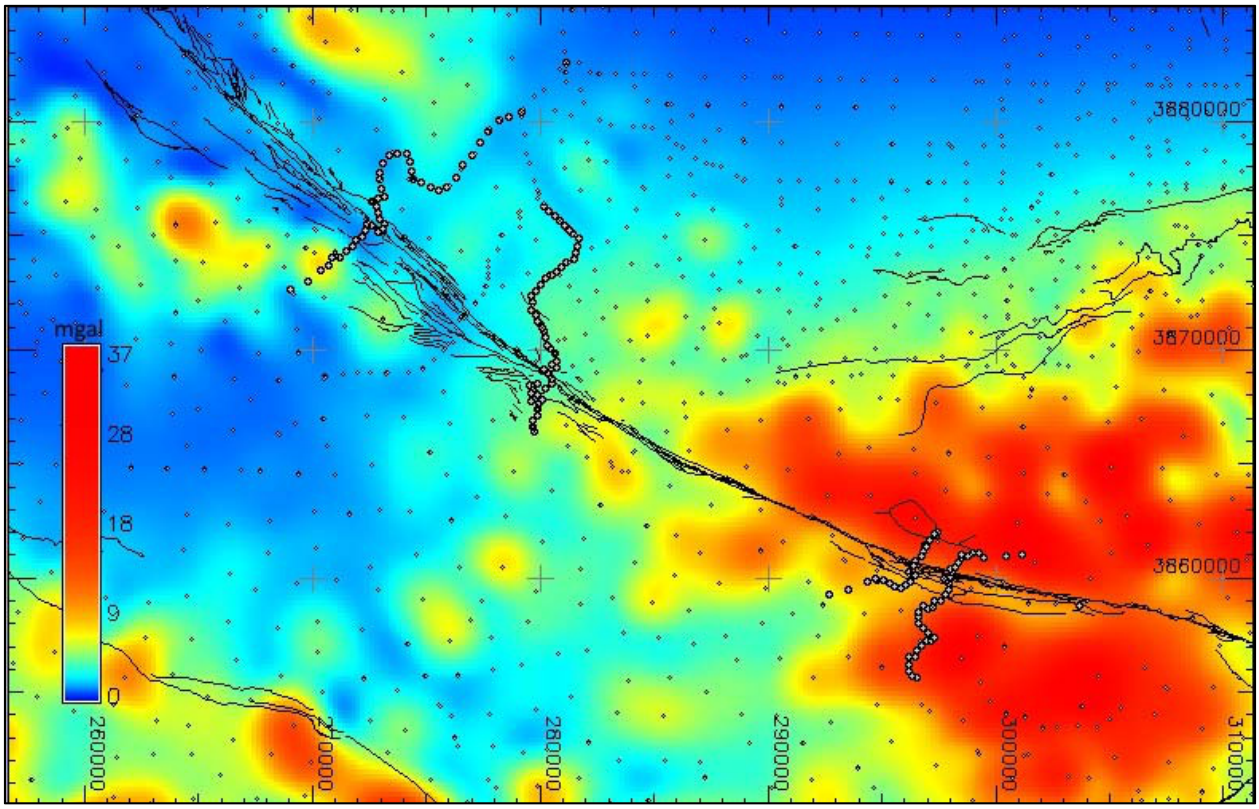

Figure 2.3. Terrain correction values map of the field work area. (Stations are shown as circles.)

In this study, pre-existing University of Texas El Paso terrain correction data was used. Their inner and outer terrain correction values were added to create a total terrain correction value. Those values were then gridded on a map using the GRASS GIS software and sampled at the locations of gravity stations presented here (Figure 2.3). This method is less precise than conducting new terrane corrections, but the total terrane correction error estimated to be less than 1-2 mgal, and new complete Bouguer anomalies from this study agree well with previous data.

2.3.4. Spherical Cap Correction

This correction is also known as Bullard B correction and exchanges the physically inexplicable slab model of the Earth and converts its shape to a more realistic one. For the spherical

cap correction, we used Bullard B coefficients from Nowell, 1999.

After applying each of these above correction steps respectively, a final complete Bouguer anomaly was determined. Complete Bouguer anomaly is acquired by adding terrain corrections to the simple Bouguer anomaly.

CHAPTER 3

RESULTS

Presented here are 166 new gravity stations as previously stated. Most of those stations (all but the base stations) were on the four main transect that are perpendicular to the San Andreas Fault. In this section, a closer look will be taken at the results from the high resolution gravity transects and they will also be compared to pre-existing data. Pre-existing data is from the University of Texas El Paso National Gravity database. The results have three graphics from each transect and that three graphics are: the Free-air gravity anomaly, the simple Bouguer gravity anomaly, and the complete Bouguer gravity anomaly respectively. The results will start from the southernmost transect (Apache Saddle) and continue to northward. The last one will be the Elkhorn Grade Road transect which is the northernmost transect. It should be stated that the gravity station points have been re-projected on to a linear line to maintain geometrical accuracy.

3.1. Apache Saddle Transect

First the Free-Air gravity anomaly values of the Apache Saddle transect are examined (Figure 3.1). The gravity values on this transect were originally collected from south to north (S-N) direction. The Free-air gravity anomaly is generally changing with the elevation but elevation is not the only factor. The density of the rocks beneath the gravity stations also affect the Free-air gravity anomaly values. Less dense rocks cause lower Free-air gravity anomalies. Apache Saddle transect has higher density crystalline basement rocks on the both ends and those rocks cause high Free-air gravity anomaly values. The lower Free-air gravity anomaly values in this graphic caused by the San Andreas Fault zone (the fault and the fault gouge) and the sedimentary rocks next to the San Andreas Fault.

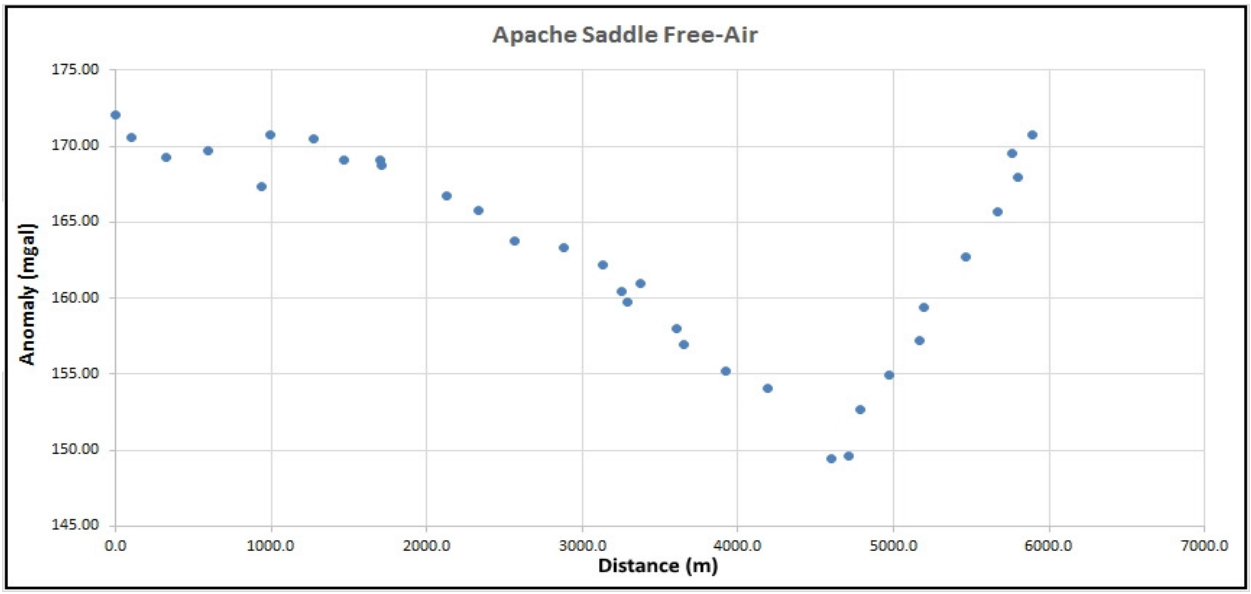

Figure 3.1. Free-Air anomaly graphic of Apache Saddle Transect

Bouguer gravity anomaly values depend on the landmass/bodies above the ellipsoid/and under the gravity station. Also it needs to be remembered this values do not contain terrain corrections. It is clear that near sedimentary rocks caused lower Bouguer gravity values on both ends of this transect whereas in the middle section Bouguer gravity values are higher due to the denser rocks and the uplift of the basement rocks (Figure 3.2).

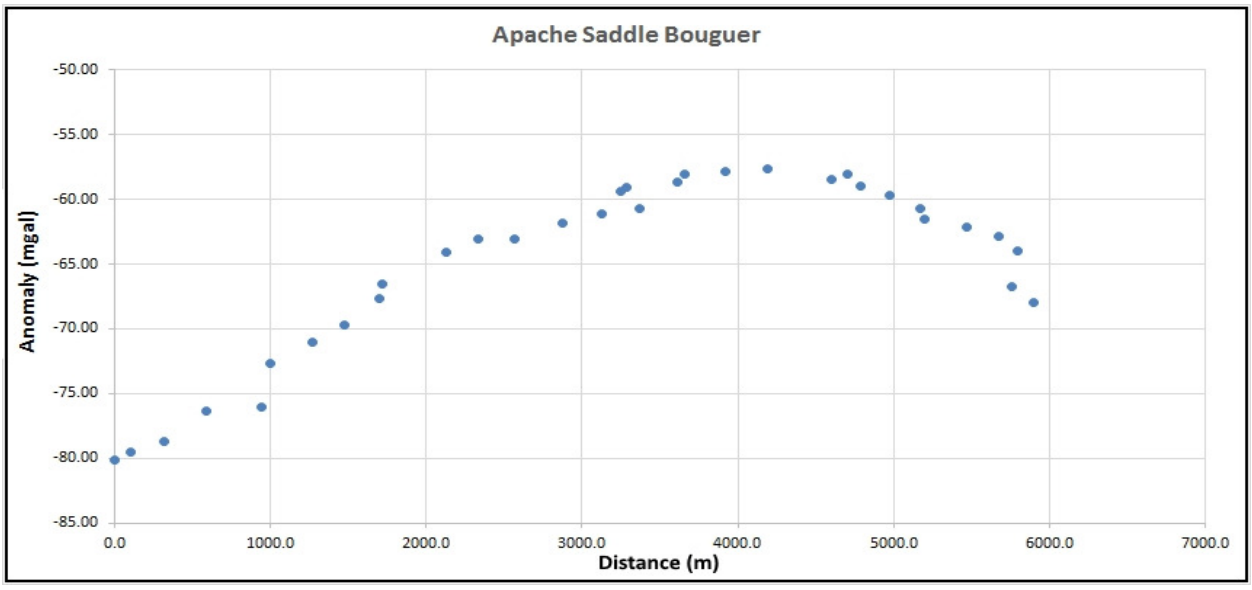

Figure 3.2. Simple Bouguer anomaly graphic of Apache Saddle Transect

When the necessary terrain corrections were applied to the Bouguer gravity values, this results in a better graphic that shows the complete Bouguer gravity anomalies on this transect (Figure 3.3) In the field, this transect began on a hill and then went downwards to the Apache Saddle fire station on the Hudson Ranch Road (this road is very close to the San Andreas Fault's main strand and lies parallel to the fault). After we continued to go uphill to finish the transect. However, it should be noted that all the points of this transect are on the mountain range and elevation does not change dramatically. At the beginning of this transect the effects of sedimentary rocks off the mountain range can be observed as relatively lower gravity values. Also the basement rocks in this part have lower density than the ones at the end of transect. This also caused lower gravity values on the south than the north. Once we past the relatively less dense basement rock location, gravity values are starting to increase due to very dense Proterozoic rocks. After the Proterozoic rocks, gravity values are generally changing in a 5 mgal band. This relatively higher gravity values are due to uplift of the high density basement rocks.

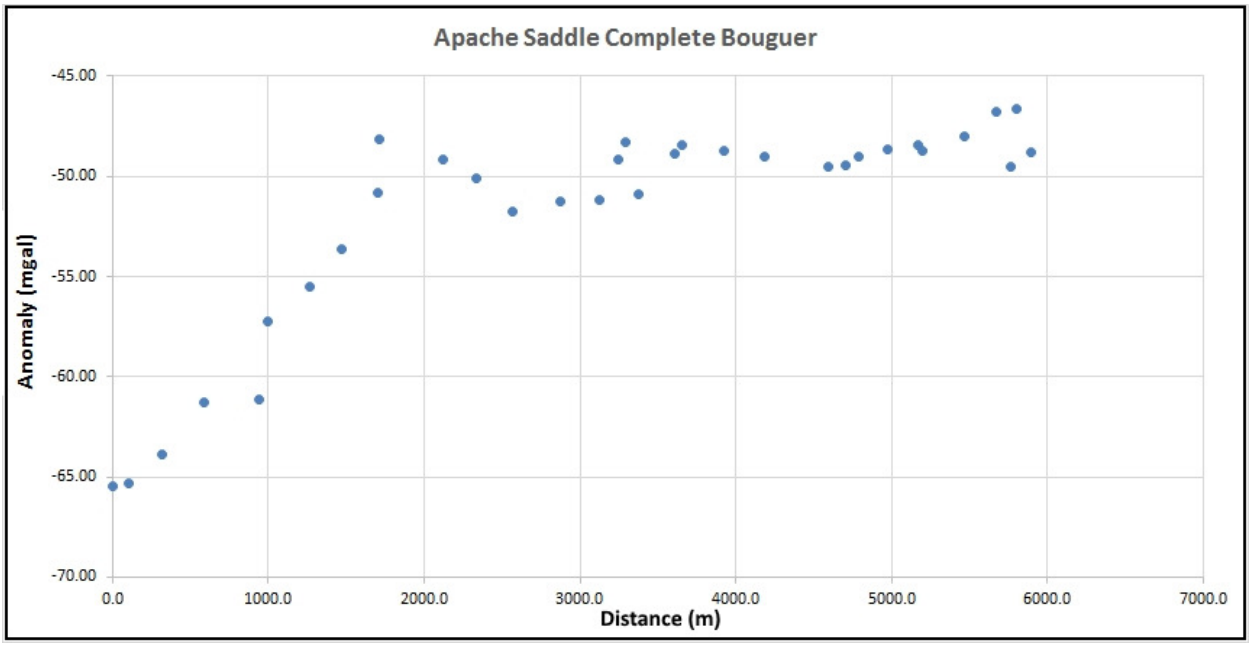

Figure 3.3. Complete Bouguer anomaly graphic of Apache Saddle Transect

3.2. Forest Road 27 Transect

Forest Road 27 is the next transect after the Apache Saddle. The gravity values on this transect were originally collected from north to south (N-S) direction, opposite of the direction of Apache Saddle transect but to make sure all transects have the same direction we made the required changes. In field work, we started this transect on the hill north of the San Andreas Fault. Then we drove downhill to the Hudson Ranch Road, after this point transect went into a small valley.

When we look at the Free-air gravity anomaly values graphic, we can see a good combination of elevation and rock density effect (Figure 3.4). The transect starts at the lowest elevation where sedimentary rocks are abundant, unsurprisingly this caused low free-air gravity anomaly values. From there gravity stations continued to uphill where crystalline basement rocks are abundant. This increase in elevation and density leads to higher free-air gravity anomaly values.

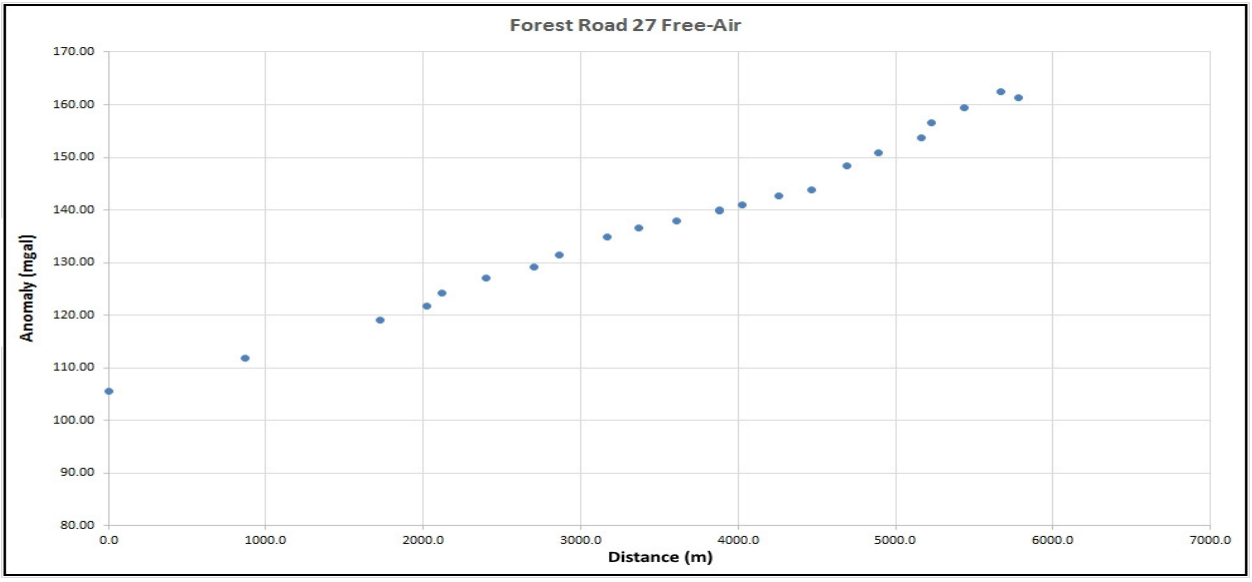

Figure 3.4. Free-Air anomaly graphic of Forest Road 27 Transect

Bouguer gravity anomaly graphic of Forest Road 27 transect is a good example of how simple Bouguer gravity values might be deceptive (Figure 3.5). At the beginning of transect, higher

simple Bouguer gravity anomaly values can be seen. Yet, that part is actually where sedimentary rocks overlie basement rocks in the valley and should have lower density values. Without terrain corrections, simple Bouguer correction may assume that valley is occupied with rock that would apply a downward gravitational pull. This correctional mistake is the reason of high simple Bouguer gravity anomaly values. Same problem also applies to the other end of this transect. This time topographic mass above the gravity station applies an upward pull in gravity meter. So it is safe to say that interpretations of simple Bouguer gravity anomaly values for this transect might lead to very wrong outcomes.

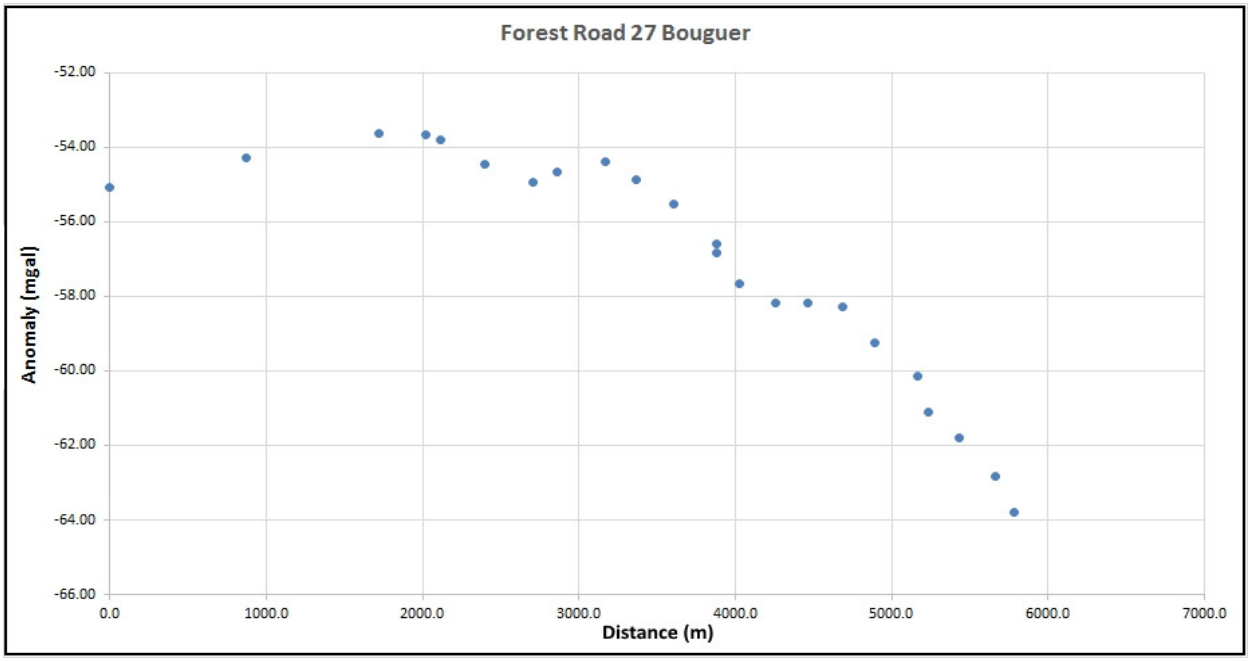

Figure 3.5. Simple Bouguer anomaly graphic of Forest Road 27 Transect

After applying the necessary terrain corrections, we have a way better graphic of complete Bouguer gravity anomaly values of Forest Road 27 transect (Figure 3.6). Sedimentary rocks at the beginning of the transect give lower complete Bouguer gravity anomaly values, whereas on the other end crystalline basement rocks give higher complete Bouguer gravity anomaly values. Minimum point in this graphic is caused by the San Andreas Fault zone and the low density fault

gouge.

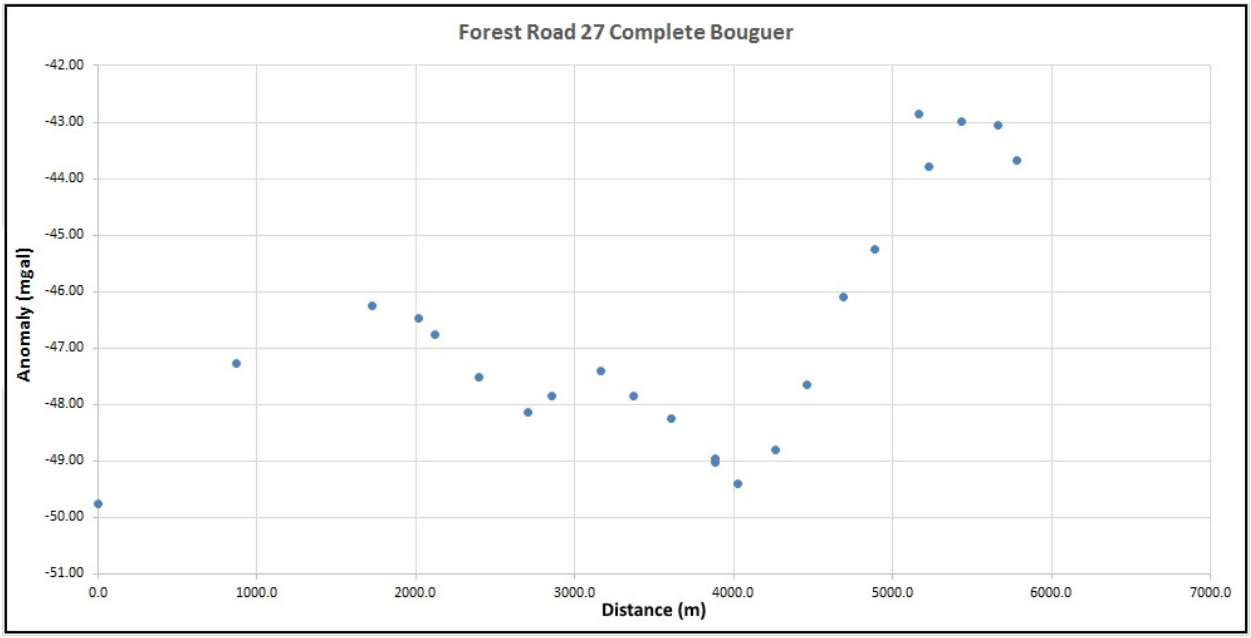

Figure 3.6. Complete Bouguer anomaly graphic of Forest Road 27 Transect

3.3. Klipstein Canyon Road Transect

The next transect is Klipstein Canyon Road transect. The gravity values on this transect were originally collected from south to north (S-N) direction. Starting point of this transect is on the Hudson Ranch Road but we only got several gravity stations over there and entered the Klipstein Canyon Road for the rest of the transect. Then we finished this transect at the intersection of Klipstein Canyon Road and US Highway 166.

The first graphic for this transect is free-air gravity anomaly values graphic (Figure 3.7). In this transect, the free-air gravity anomaly values are dramatically decreasing from start to end due to the change in elevation. Starting point is on the hills of the canyon and from there we continue all the way to the bottom of the canyon. As expected lower elevation gives us lower free-air anomaly values.

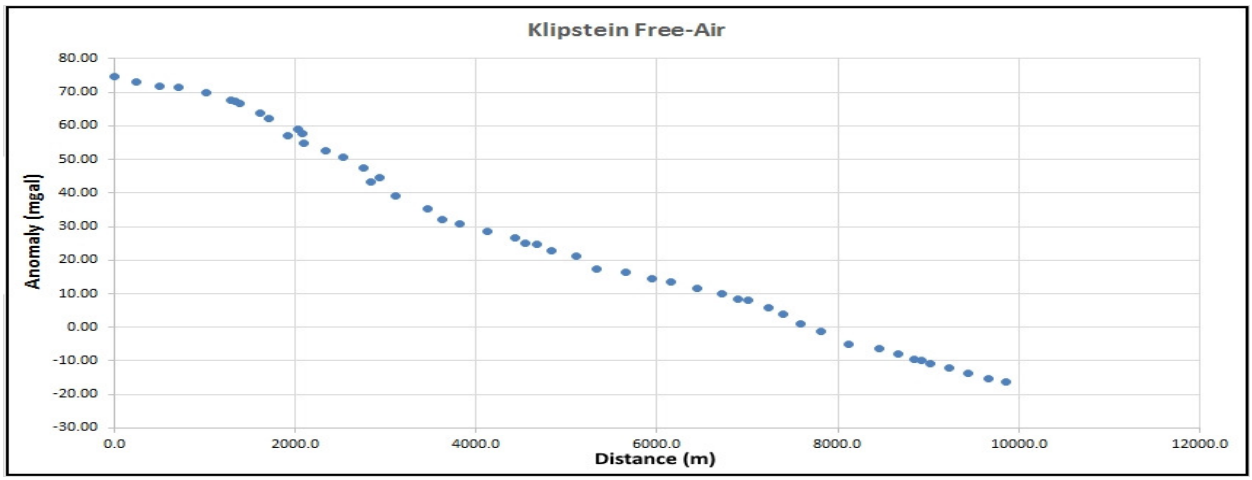

Figure 3.7. Free-Air anomaly graphic of Klipstein Canyon Road Transect

The simple Bouguer gravity anomaly values graphic gives us a good idea about the beginning of the transect where sedimentary rocks overlie basement rocks yet basement rocks are getting thicker when we get closer to the San Andreas Fault and it causes an increase in gravity (Figure 3.8). The San Andreas Fault can be located in this graphic right before the simple Bouguer gravity anomaly curve reaches minimum. After the fault we have a zone of lower density siltstones and shales. This zone keep gravity low for a while but after some point we have relatively denser sedimentary rocks and also the effect of basement rocks is more detectable.

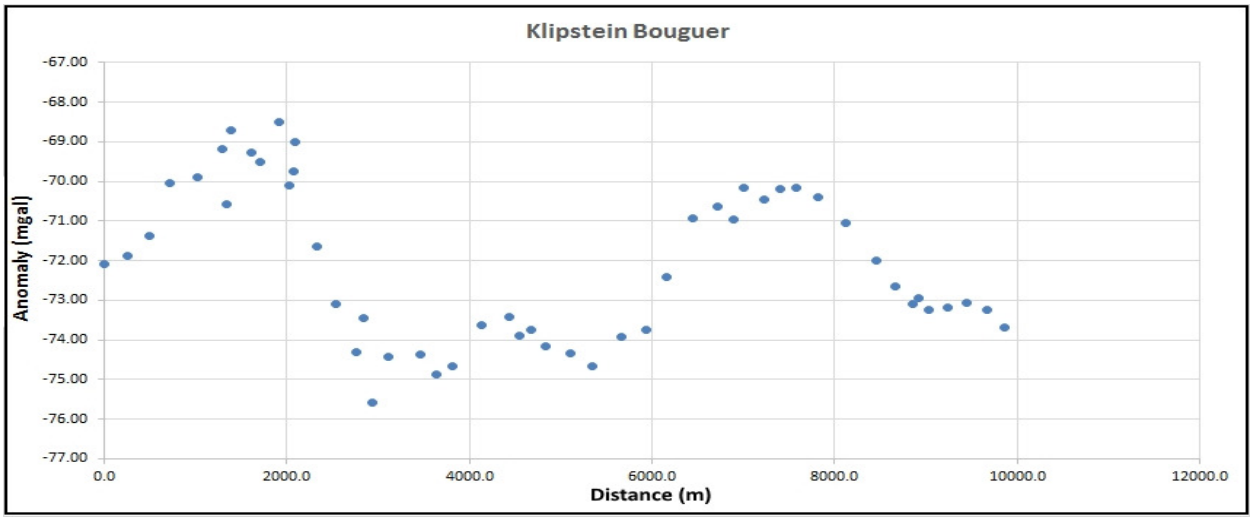

Figure 3.8. Simple Bouguer anomaly graphic of Klipstein Canyon Road Transect

The complete Bouguer gravity anomaly values graphic for Klipstein Canyon Road is almost identical to simple Bouguer gravity anomaly values graphic. Terrain correction effect causes an increase in gravity by several mgal (Figure 3.9).

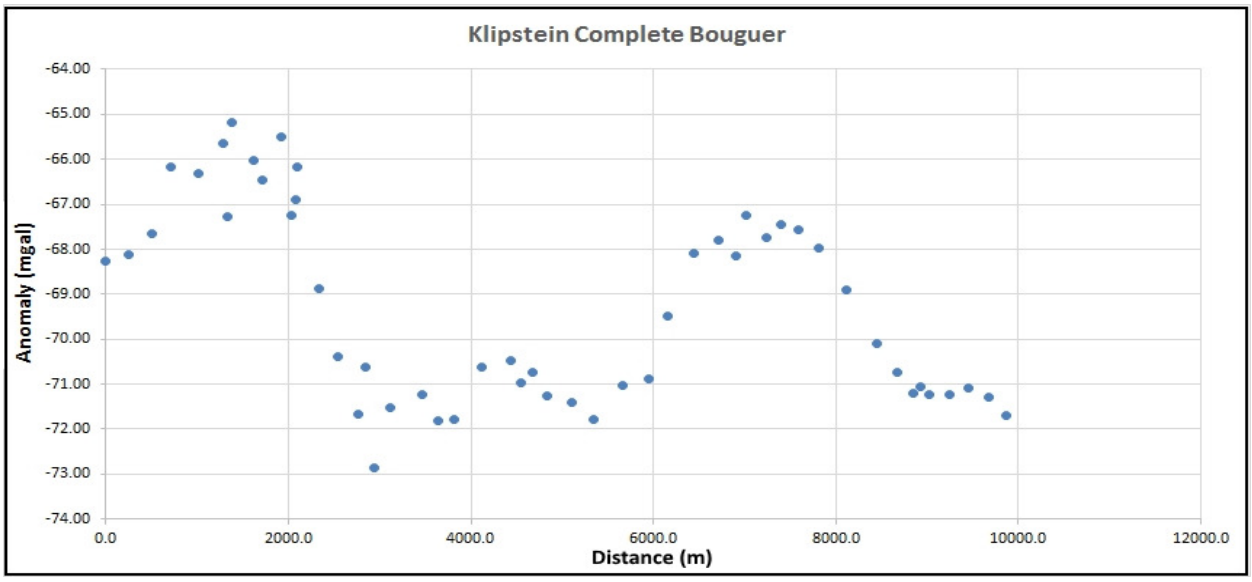

Figure 3.9. Complete Bouguer anomaly graphic of Klipstein Canyon Road Transect

3.4. Elkhorn Grade Road Transect

The last and the southernmost transect is Elkhorn Grade Road transect. The gravity values on this transect were originally collected from north to south (N-S) direction but to make sure all transects have the same direction we made the required changes. This transect starts on the southern end of the Carrizo Plains. Once we passed the San Andreas Fault, we started to go into the hills of Elkhorn Grade Road. End point for this transect is at the intersection of Elkhorn Grade Road and US Highway 166.

The first graphic is the free-air gravity anomaly values graphic of the Elkhorn Grade Road (Figure 3.10). Like in the Klipstein Canyon Road transect, main reason for the dramatic decrease in the free-air gravity anomaly values is elevation change.

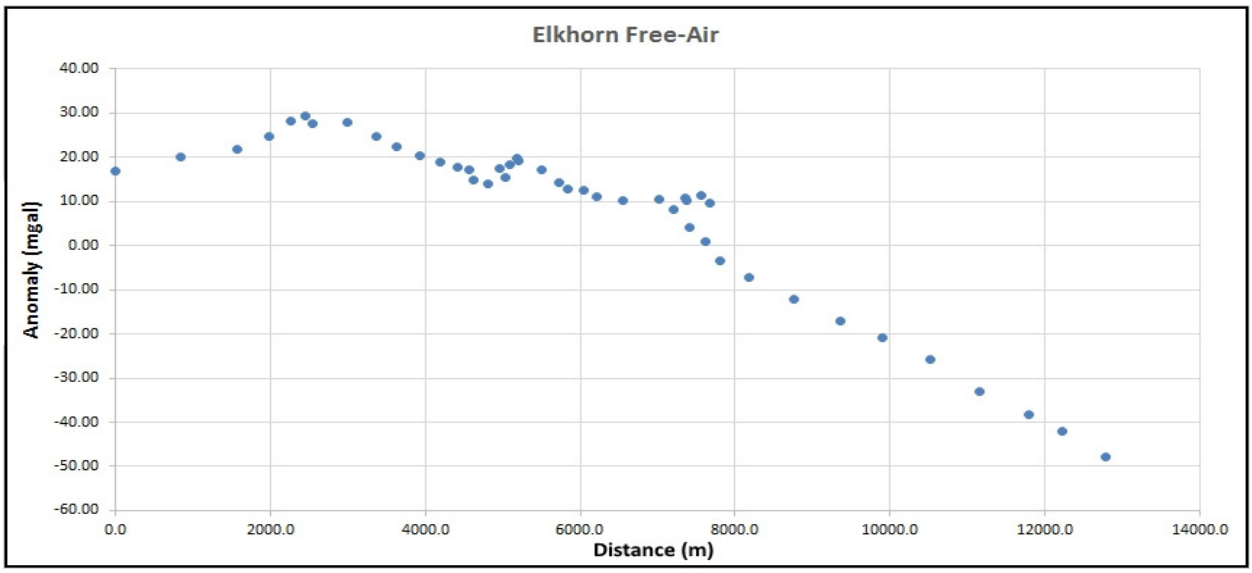

Figure 3.10. Free-Air anomaly graphic of Elkhorn Grade Road Transect

The simple Bouguer gravity anomaly values graphic gives us a reasonable insight for this transect (Figure 3.11). The San Andreas Fault is located right before the gravity curve reaches around -82 mgal. This low gravity curve caused by low density sedimentary rocks deposited in the area. After the fault some igneous bodies caused an increase in gravity and it is apparent in the graphic. Then we entered a low density sedimentary rock zone again and these sedimentary rocks getting thicker when we move to the end of transect. This thickening in the sedimentary rocks caused a visible decrease in the gravity.

Complete Bouguer gravity anomaly values graphic of Elkhorn Grade Road is similar to the simple Bouguer gravity anomaly graphic (Figure 3.12). However, there is a difference for the part before the San Andreas Fault. There is an apparent increase in the middle of this part and this increase might be caused by igneous cobbles or a local uplift of basement rocks. Except that the necessary terrain corrections cause an increase in gravity by couple mgals.

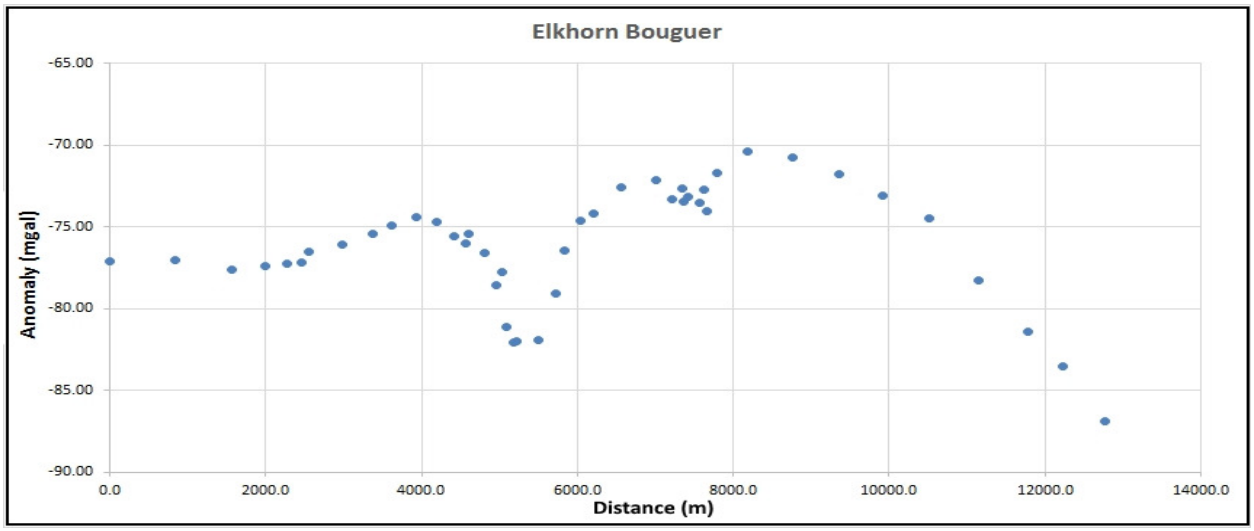

Figure 3.11. Simple Bouguer anomaly graphic of Elkhorn Grade Road Transect

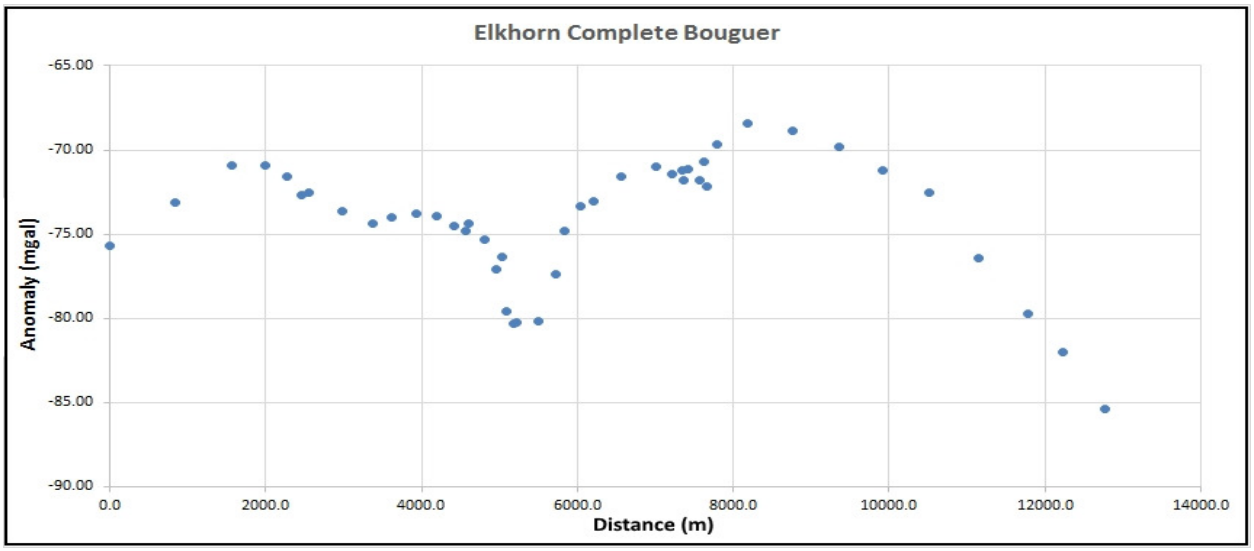

Figure 3.12. Complete Bouguer anomaly graphic of Elkhorn Grade Road Transect

3.5. Data Comparison

This field work is not the first gravity survey in the area. There are many pre-existing gravity data but the gravity stations are distributed far from each other and their spatial resolution is not very good. With this survey high resolution gravity data were collected on the both ends of the Big Bend of the San Andreas Fault. It is easier to explain the difference between the new data and pre-existing data when we compare them on graphics.

First graphic indicates the results for the Apache Saddle transect (Figure 3.13). At the beginning of this transect, we have lower gravity values due to the effects of sedimentary rocks and relatively lower density basement rocks. After the first couple kilometers in this transect our data gives higher gravity values because of the oldest and densest basement rocks in the area. Also gravity values in pre-existing data stay stable after the middle of transect. However, our high resolution gravity survey indicates lower gravity values due to the San Andreas Fault gouge zone and sedimentary rocks in that part of the transect.

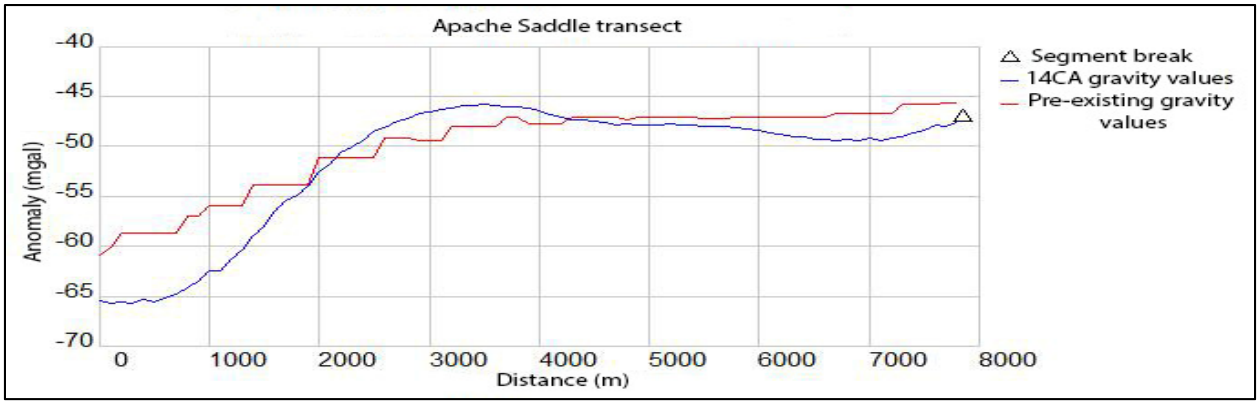

Figure 3.13. Data comparison for Apache Saddle Transect

The second graphic shows the results for the Forest Road 27 transect (Figure 3.14). In first couple kilometers both data have similar gravity values but after that point our data gives better resolution for the low density fault gouge and sedimentary rocks.

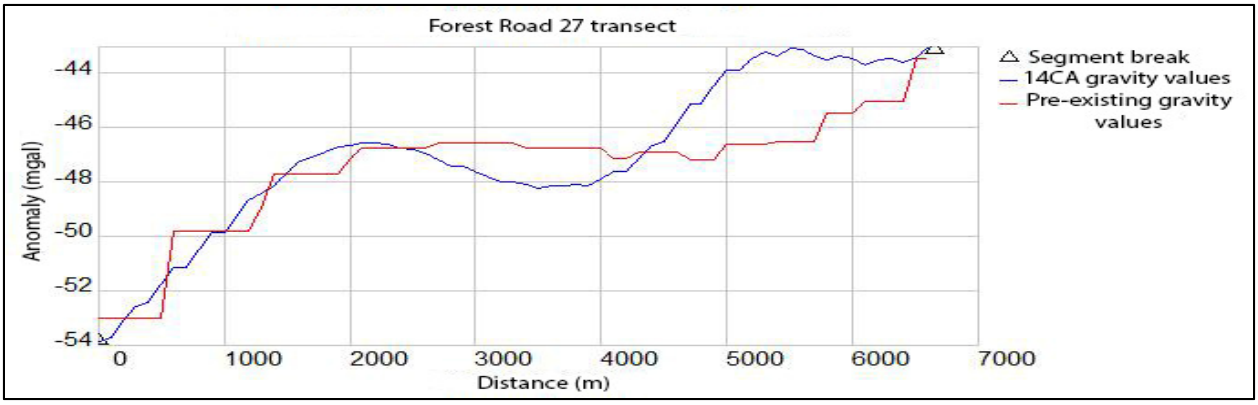

Figure 3.14. Data comparison for Forest Road 27 Transect

The third graphic shows the results for Klipstein Canyon Road transect (Figure 3.15). Both data have similar results except for the locations of low density fault gouge zones and uplifted basement rocks. It is clear that our data has better resolution for the important locations of the profile.

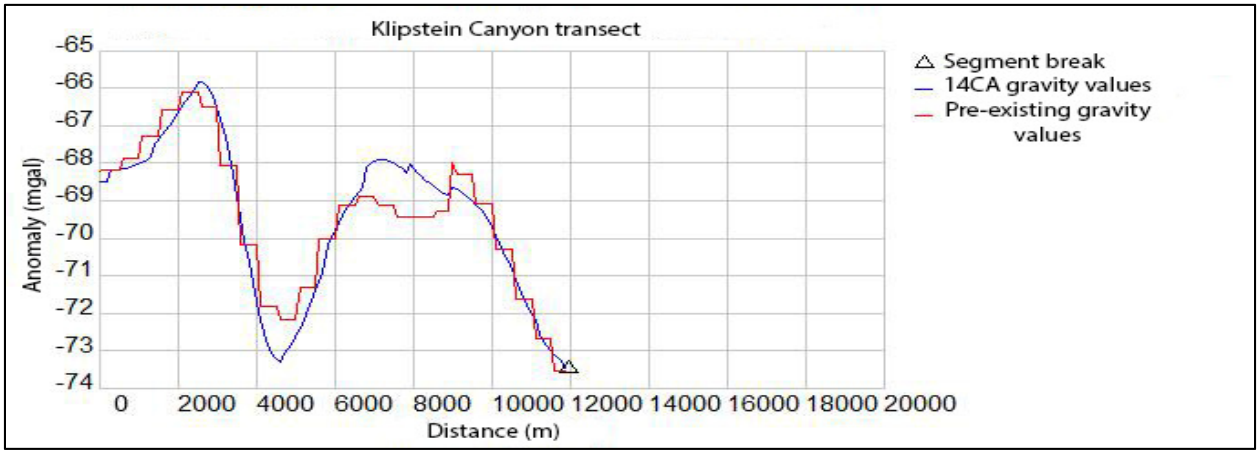

Figure 3.15. Data comparison for Klipstein Canyon Road Transect

The last graphic shows the results for Elkhorn Grade Road transect (Figure 3.16). Pre-existing and newly collected data have almost identical values in this transect. Only difference is right before the middle of transect our data points out the low density sedimentary rocks better.

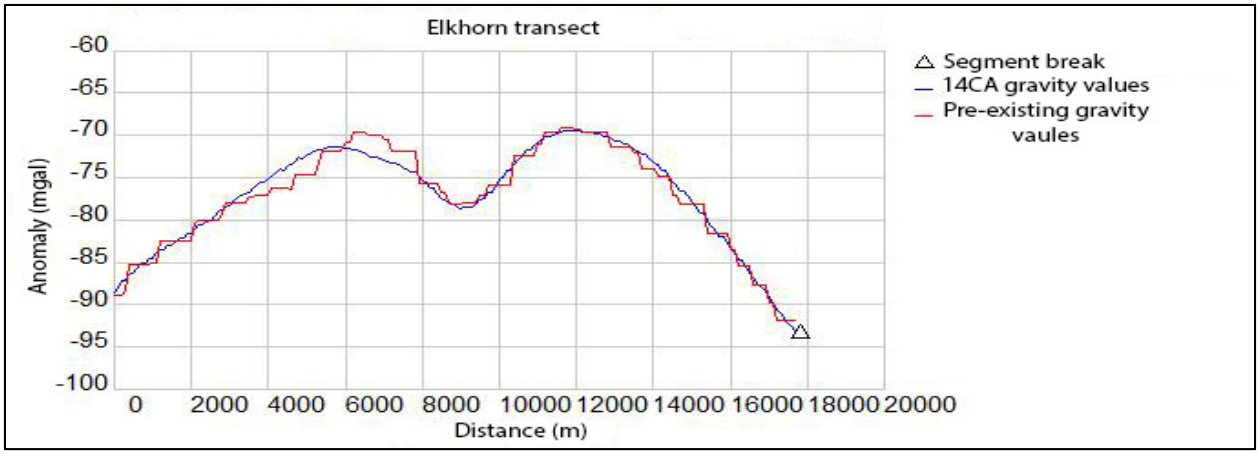

Figure 3.16. Data comparison for Elkhorn Grade Road Transect

CHAPTER 4

STRUCTURAL MODELS

Creating structural models of this complex and geologically important area is one of the most important goals of this thesis. With the modeling process, the geometry of the San Andreas Fault in the Big Bend area can be better understood. Also this process yields a better understanding of the subsurface geology in the area. In this chapter, the models generally rely on observations and samples from the field work presented here. Density measurements of rock samples were carefully made in the laboratory. During field work, samples were collected from relevant rock units in addition to the gravity survey. However, previous geologic studies and rock densities were used as needed.

The next step was generating the structural models. The GRAVMAG program was used for the modeling process. GRAVMAG is a software that helps users to analyze gravity and/or magnetic (only gravity data was used in this study) data gathered along a profile. It is a two-dimensional (2-D) gravity modeling program. It is very useful for testing how subsurface bodies would affect observations made on the surface. GRAVMAG presumes that bodies under the profile continue to infinite distance perpendicular from the profile. In the software, the "Gravity Data Window" was used to upload the gravity data along a profile. Then in the "Model Window" we add bodies, set their densities and edit them precisely. Finally, the "Section Window" was used to see bodies, cross-section, and the gravity data. The data shows up as "observed gravity" in the "Section Window". Every change made in the "Section Window" affect the "calculated gravity" which is generated by bodies in the "Model Window". The best result was achieved when "calculated gravity" and "observed gravity" lines are on top of each other.

Four structural models were created for this thesis work. Two of those models are on the southern end of the Big Bend of the San Andreas Fault and two of them are on the north of it. To make models easier to understand and focus more on the near surface geology, 50 mgal was subtracted from every gravity observation have been made in the field work. Three of the models have 5 km depth and one of them has a 7 km depth. Orientation of the models is from south to north (S-N) for all of them. Interpretation of structural models will proceed from the southernmost profile and finish with the northernmost profile.

4.1. Structural Model A-A' (Apache Saddle)

This cross section is the southernmost of the four. This model has 7 km depth and 12 km length. This profile is dominated by basement rocks and almost all basement rocks are separated from each other with faults (Figure 4.1). Crystalline basement rocks form a flower structure bounded by high angle reverse faults. This profile starts with Pliocene to Oligocene terrestrial sedimentary rocks which is overlying Cretaceous crystalline basement rocks. After this sedimentary unit we observe a long line of Cretaceous to Proterozoic crystalline basement rocks on the surface. Only exception is the Sawmill Mountain fault between the Rand Schist and Cretaceous Granite. Sawmill Mountain Fault is the other fault that has fault gouge zone in this profile with the San Andreas Fault. Both of these faults are dipping to southwest with approximately 75°. Right before the San Andreas Fault, there is a vertically extensive sedimentary rock unit. This sedimentary unit mostly consists of upper to middle Miocene rocks of Caliente Formation. On the north of the San Andreas Fault, there is yet another vertically extensive sedimentary rock unit which consists of lower Miocene to upper Oligocene rocks of Temblor Formation. Next to the Temblor Formation, we have a body of Mesozoic metasedimentary rocks. Temblor Formation and Mesozoic metasedimentary rocks are separated by a reverse fault. This

Mesozoic metasedimentary unit overlies the Cretaceous Granite.

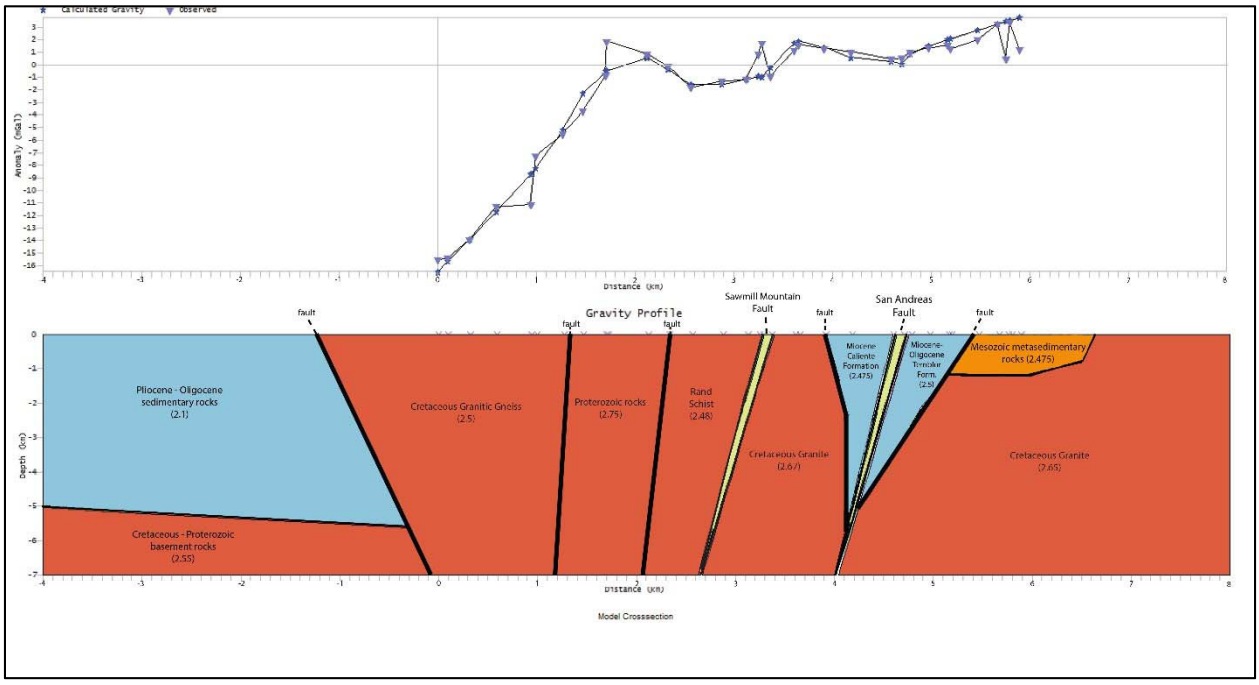

Figure 4.1. Model Cross-section A-A'. (Values in parentheses represent density in gr/cm^3)

4.2. Structural Model B-B' (Forest Road 27)

The next model belongs to the Forest Road 27 profile. This model has 5 km depth and 10 km length (Figure 4.2). Like the last one, this profile is also mostly dominated by the crystalline basement rocks. There are two sedimentary rock units on the south of the San Andreas Fault. Both of these sedimentary units are upper to middle Miocene rocks of Caliente Formation and overlie on the Cretaceous to Proterozoic crystalline basement rocks. Both units of sedimentary and basement rocks are separated by a low density fault gouge zone. This fault uplifted the basement rock by couple hundred meters on the south of it. After the San Andreas Fault gouge zone we observe lower Miocene to upper Oligocene sedimentary rocks of Temblor Formation. Temblor Formation is vertically extensive in this model like in the prior model. Then there is another uplifted high density Cretaceous Granite body which has a fault gouge zone in it. This granite body is overlain by a Pliocene to Oligocene marine sedimentary rock unit on the very north of this

profile. It should be noted that this marine sedimentary unit is extensively folded. The San Andreas Fault is dipping to southwest with approximately 85° in this model.

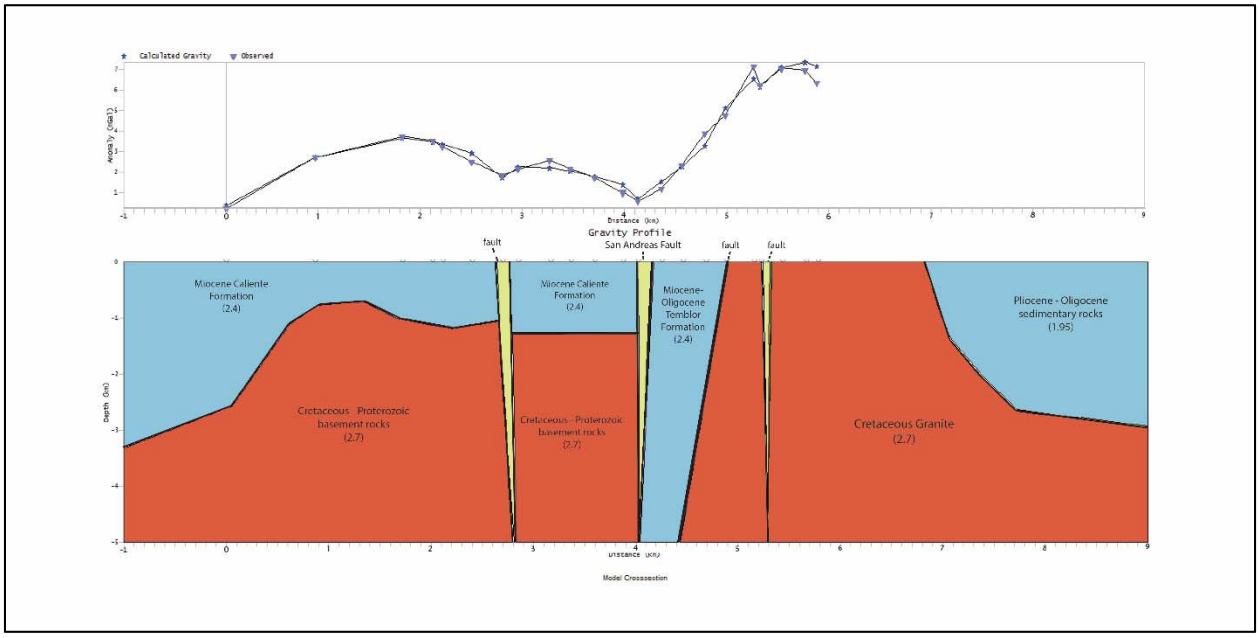

Figure 4.2. Model Cross-section B-B'. (Values in parentheses represent density in gr/cm^3)

4.3. Structural Model C-C' (Klipstein Canyon Road)

The third model belongs to the Klipstein Canyon Road profile. This model has 5 km depth and 15 km length (Figure 4.3). This profile is important because it represents the end of uplifted basement rocks area. All units are continuous and traceable from Apache Saddle profile until this profile. From this point geology is changing drastically. On the south of the San Andreas Fault, there is a sedimentary unit overlie Cretaceous to Proterozoic crystalline basement rocks. This sedimentary unit consists of Oligocene rocks of Simmler Formation, lower Miocene rocks of Vaqueros Formation and Pliocene to lower Miocene rocks of Caliente Formation from bottom to the top. Both sedimentary rocks and basement rocks on the south of the fault have great amplitude of folding. Between the San Andreas Fault gouge zone and the fault gouge zone on the very north, there are apparent anticline and syncline structures. These two faults also uplifted the crystalline

basement rocks and generate a flower structure. In this area, sedimentary rocks units consist of middle Eocene rocks of Live Oak Formation, Oligocene rocks of Pleito Formation, lower Miocene to upper Oligocene rocks of Temblor Formation and upper Miocene rocks of Bitterwater Creek Shale from bottom to the top. These sedimentary units are separated by faults. After the northernmost fault in this profile, we observe a sedimentary unit which consists of lower Miocene to Oligocene rocks of Temblor Formation and upper to middle Miocene rocks of Monterey Shale. This sedimentary unit overlain by low density Quaternary alluvial deposits. Under the sedimentary unit we have another Cretaceous to upper Paleozoic crystalline basement rock unit. This model suggests a northward dip of approximately 80° for the San Andreas Fault.

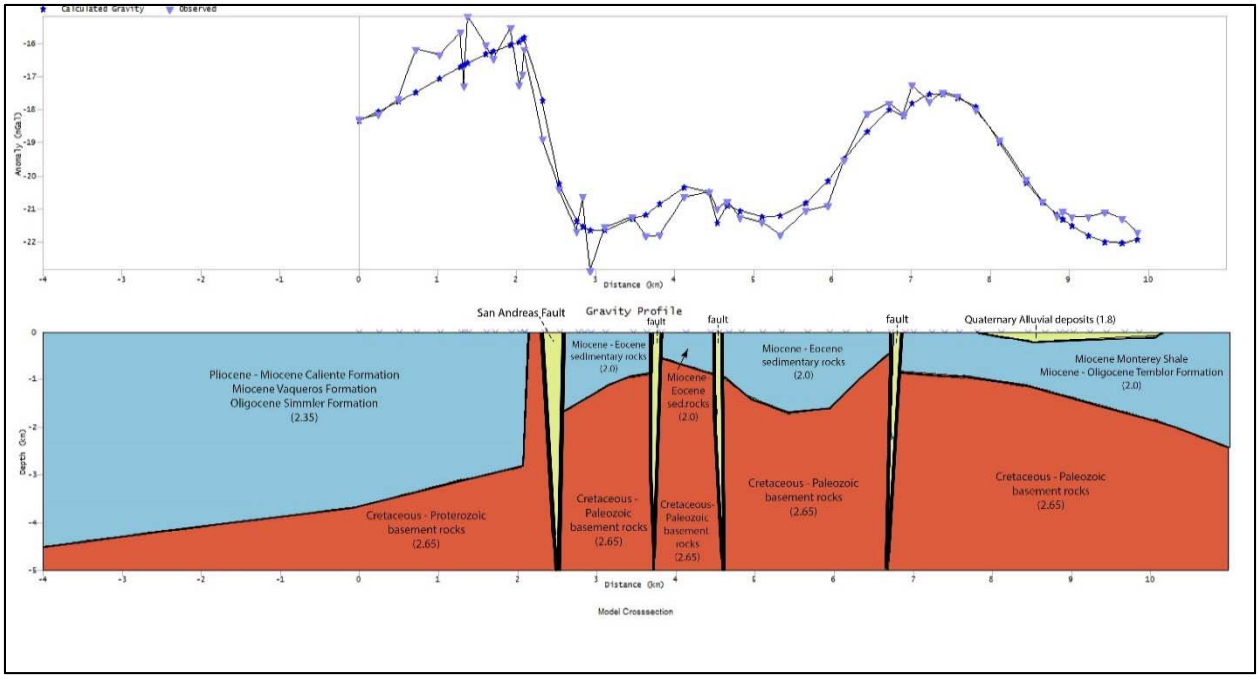

Figure 4.3. Model Cross-section C-C'. (Values in parentheses represent density in gr/cm^3)

4.4. Structural Model D-D' (Elkhorn Grade Road)

The northernmost model is along the Elkhorn Grade Road profile. This model has a 5 km depth and 18 km length (Figure 4.4). This profile starts with a sedimentary unit that consists of Quaternary alluvial deposits and Pliocene rocks of Paso Robles Formation. In the middle of this

sedimentary unit, there is a sliver of high density Miocene basalt unit. The San Andreas Fault has a fault gouge zone in this area but it is mixed with Quaternary Lacustrine deposits. Between the San Andreas Fault and the Recruit Pass Fault, there is a sedimentary unit which consists of upper Miocene rocks of Bitterwater Creek Shale, upper Miocene rocks of Santa Margarita Formation and these rocks unconformably lie on upper and middle Miocene rocks of Monterey Shale. According to our model, there is a high density body in between Bitterwater Creek Shale and Santa Margarita Formation at some point. This high density body might be coarse grained alluvial fan deposit yet we are not sure exactly what it is.

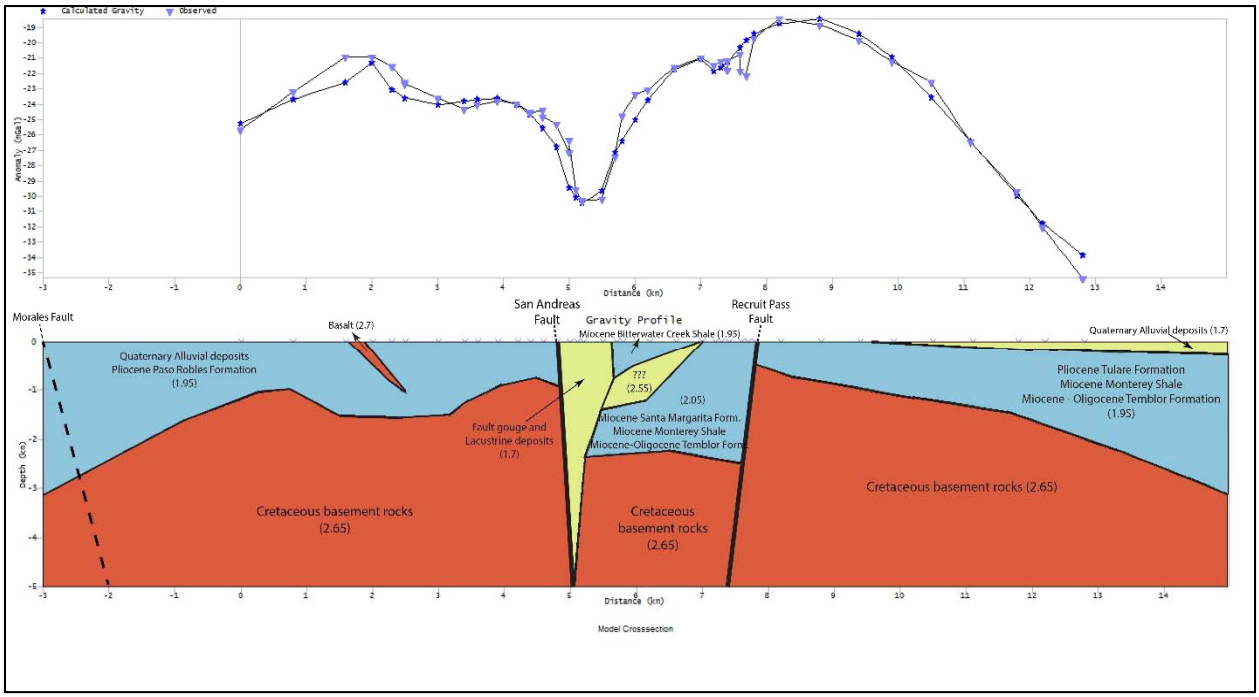

Figure 4.4. Model Cross-section D-D'. (Values in parentheses represent density in gr/cm^3)

After the Recruit Pass Fault, there is another sedimentary rock unit is overlain by Quaternary alluvial deposits. This sedimentary unit consists of lower Miocene to Oligocene rocks of Temblor Formation, upper and middle Miocene rocks of Monterey Shale and Pliocene rocks of Tulare Formation from bottom to the top. Also this sedimentary unit is getting thicker to the north

and has a huge amplitude of folding. The remarkable point of this profile is the precise flower structure that caused by the motion of the San Andreas Fault and the Recruit Pass Fault. Our model suggests a northeastward dip of approximately 80° for the San Andreas Fault and a southwestward dip of 80° for the Recruit Pass Fault.

CHAPTER 5

DISCUSSION

5.1 Gravity Model Tectonic Implications

The main goal of this thesis is to use gravity measurements combined with geologic observations to better understand the curvature of the San Andreas Fault in the Big Bend and its role in producing hydrocarbon bearing structures in the southern Central Valley of California. There are many pre-existing gravity data in the area but the problem is pre-existing data sets do not have the needed local density of spacing. However, the gravity survey presented here specifically focused on the Big Bend of the San Andreas Fault and the spacing between most of our stations is 0.3 kilometers. All four of the gravity transects are perpendicular to the San Andreas Fault, and so give us a good comparison of the rocks and structure on the either side of the SAF itself.

As stated the goal of this project is to better determine the geometry of the San Andreas Fault in the Big Bend area. The geometry of the San Andreas Fault in the Big Bend has been strongly debated and there are many studies regarding this topic. The main result of the gravity models from this study is that flower structures centered on the San Andreas Fault are present along each profile. In the two southern models, crystalline basement rocks are exposed in the core of a positive flower structure. The Klipstein Canyon Road profile presents a similar positive flower structure, but it is covered folded sedimentary cover. The northernmost Elkhorn Grade Road profile structurally different and contains a negative flower structure in which the central block is down dropped greater than 1 km. The down dropped central block along the Elkhorn Grade Road profile is consistent with the structural surface mapping of Arrowsmith (1995) particularly with regard to the existence of extensional structures such as grabens and normal faults. The down

dropped central block provides a large-scale mechanism for such small-scale geologic surface structures. The down dropped central block also provides a good explanation for the existence of the Carrizo Plains themselves. Finally, the down dropped block indicates that the amount of contraction across the San Andreas Fault at Elkhorn Grade Road is much less than the southern transects that this additional contraction is due to the Big Bend itself.

One of the previous studies (Fuis et al., 2012) suggests that the San Andreas Fault has a propeller like shape in southern California, and is moderately dipping to southwest with 55° in the Big Bend area. Yet, the structural models presented here suggest otherwise. As shown in the previous chapter, the four structural models across the San Andreas Fault all suggest that the fault is steeply dipping with minor variations. On the south end of the Big Bend, the first and southernmost model (A-A') shows that the San Andreas Fault is dipping to southwest at approximately 75°. The second model (B-B') suggest a southwestward dip of approximately 85° for the San Andreas Fault. On the north end of the Big Bend, the model (C-C') suggests a northward dip of approximately 80°. The last and northernmost model (D-D') indicates that the San Andreas Fault is dipping to the northeast at approximately 80°. Fuis et al., 2012 paper suggests a lower angle for the dip of 55° along the San Andreas Fault in the Big Bend, but the models constructed for this thesis indicate near vertical SAF dip angles in this region.

Another point that the models constructed for this thesis suggest different than previous studies is regarding the existence of the Abel Mountain thrust. Kellogg and Miggins (2002) made a geologic mapping of the Sawmill Mountain quadrangle. They hypothesized a shallow, low angle Abel Mountain thrust in which crystalline basement rocks were thrust over the Miocene Caliente Formation in their A-A' cross section for a distance of several kilometers. This cross section is very close to the Apache Saddle transect. The Apache Saddle transect gravity model (A-A') does

not support the existence of a near horizontal thrust sheet. Instead, the model indicates that the crystalline basement rocks are vertically extensive in the area. Overall, the model suggests the Cretaceous to Proterozoic basement rocks form a positive flower structure bounded by high angle faults with a significant reverse component.

A final tectonic implication of the gravity models has to do with the total amount of exhumation along the SAF in the Big Bend. Along the north side of the Big Bend, the Klipstein Canyon Road model (C-C') indicates a sedimentary section thickness of approximately 4 km. In the southernmost Apache Saddle transect (A-A'), that sedimentary section has been completely removed and the underlying crystalline basement rocks are exposed. In addition, the Apache Saddle transect sits at an elevation that is approximately 1 km higher than the Klipstein Canyon Road transect. Therefore, the minimum exhumation of the Apache Saddle crystalline rocks with respect to Klipstein Canyon is 5 km.

If the initiation time of uplift can be determined, then an exhumation rate can also be calculated. Previous workers have suggested that the ancestral San Gabriel Fault was transtensional, have estimated that the modern trace of the San Andreas Fault became active at approximately 5 Ma. If the onset of Big Bend uplift corresponds with the initiation of modern SAF strand slip, this suggests an exhumation rate of 1 km/Ma. This rate and timing of uplift initiation are consistent with the studies of low temperature thermochronology such as Blythe et al. (2000) and Niemi et al. (2013) who report minimum Transverse Ranges U-Th/He apatite ages of 4-5 Ma.

5.2. Gravity Model Hydrocarbon Implications

There are productive oil fields in the vicinity of our northern transects (Klipstein and Elkhorn). One of those oil fields is Cuyama Oil District in the Cuyama Valley. Cuyama Valley is a section of Salinian Block. Like the Carrizo Plains, this valley has not been uplifted. In addition,

uplifted Sierra Madre range has overridden this valley from the southwest along the South Cuyama Fault. The Caliente Range separates the Cuyama Valley and Carrizo Plain. Cuyama Oil District is in the center of the Cuyama Valley and along the west edge of the Caliente Range. The hydrocarbon deposits were discovered in late 1940s. The hydrocarbons in this oil field are ranged between heavy crude oil and light crude oil (gravity API 20°-38°). These hydrocarbon deposits are deposited in lower Miocene Vaqueros Formation, which is thicker on the northeast and thin to the southwest. Also in the South Cuyama field low amounts of oil is gathered from upper Miocene Monterey Shale. Most of the oil has been gathered in this area and now production is declining. There are some efforts to find new hydrocarbon deposits around this area and holes are drilled in numerous parts of Cuyama Valley and Caliente Range. Yet, no new hydrocarbon deposits are found.

Another big oil field in the area is the Taft Oil District. Maricopa is on the southern part of this district and also in the deepest part of the San Joaquin sedimentary basin. Taft Oil District is one of the most productive oil districts in the western United States. It is located east of the San Andreas Fault. The stratigraphy of sediments changes from Cretaceous to Quaternary in age. Quaternary alluvial deposits and Tulare Formation are terrestrial sediments of the area. Except those two, all other sediments are marine originated. Temblor and Monterey Formations can be as thick as 4.3 km in the southeast of Temblor Range. This section of the San Joaquin Basin sank very quickly in Miocene time. That is why this part is the deepest part of the basin.

The structure of the Temblor Range and Taft Oil District is associated with the right lateral drag effects of the San Andreas Fault. Regional folding developed as sedimentation occurred in the Cenozoic. Local unconformities at the bottom of Miocene Temblor and Monterey Formations suggest that local folding anticipated their distribution. Also the angular unconformity at the

bottom of upper Miocene Bitterwater Creek Shale next to the San Andreas Fault indicates that Monterey and Temblor Formations were tilted to northeast and granitic rocks were uplifted on west of the San Andreas Fault. The deformation in the area reached its peak during deposition of the Etchegoin and Tulare Formations next to the San Andreas Fault. After the deposition of Tulare Formation, the motion of the San Andreas Fault in the Quaternary tightened folds in the Temblor Range and also created new folds in the Late Cenozoic formations. Buena Vista and Elkhorn Hills anticlines are examples of those new folds. All this deformation is correlated with the time of right lateral motion of the San Andreas Fault (Harding, 1976). Tightening of pre-existing folds and creation of new ones has been uninterrupted since the Early Miocene. As a result, the structures of the Taft Oil District get more complex with depth and proximity to the San Andreas Fault.

The oil fields like Midway-Sunset, Buena Vista and Elkhorn Hills are in the southern part of the Taft Oil District. All hydrocarbons are gathered from Etchegoin and upper Monterey Formations in these oil fields. Since this area is the deepest part in the San Joaquin Basin, the hydrocarbon bearing structures in the Temblor and older formations are too deeply buried. These older formations are overlain by vast thickness of Monterey Shale and due to the pressure they are too tight to be productive.

One potential implication of the gravity models presented here with respect to the distribution of regional oil fields may come the evidence of extension along the Elkhorn Grade Road transect. All of the oil fields of the Taft Oil District occur to the east of the Recruit Pass Fault, yet the same sequence of sedimentary rocks extends across it. East of the Recruit Pass Fault the sedimentary sequence is extensively folded either by contractional deformation or via strike-slip drag folds. However, west of the Recruit Pass Fault lies the large down dropped block as shown in the gravity model (D-D'). This is also the area in which Arrowsmith (1995) reported

normal faults and graben formations. Therefore, the lack of oil fields west of the Recruit Pass Fault may be due to the change in structural style from transpression to transtension west of the fault. This suggest that transpressional tectonic regimes lead to better-developed fold structures that trap hydrocarbons, whereas in transtensional regimes (such as west of the Recruit Pass Fault) good hydrocarbon traps are less likely to form.

CHAPTER 6

CONCLUSIONS

A high resolution gravity survey in the Big Bend of the San Andreas Fault in the southern Carrizo Plains and Pine Mountain region was used to better determine the geometry of the San Andreas Fault. 166 new gravity measurements were collected for this purpose. This survey allowed for the construction of new SAF gravity constrained structural models which broaden knowledge and understanding of the Big Bend of the San Andreas Fault.

The final outcomes of this thesis are:

1. All of structural models show evidence of nearly symmetrical flower structures. These flower structures are an indicator of strike-slip motion and the contractional deformation.
2. The northernmost model (Elkhorn) exhibits characteristics of a negative flower structure whereas models to the south suggest the existence of positive flower structures centered on the San Andreas Fault.
3. There has been more than 4 km of exhumation caused by the Big Bend related faults on the southern end of the bend. Also there is approximately 1 km surface elevation change between two ends of the bend. So the total uplift is at least 5 km in the Apache Saddle/Pine Mountain region.
4. The southern transects have higher Bouguer gravity anomaly values than the northern transects due to the uplift of the crystalline basement rocks in the area.
5. Sedimentary rocks on the northern end of the bend are laterally continuous. High amplitude of folding caused by component of fault perpendicular contraction creates traps for

hydrocarbons in the area. In contrast, the transition to transtensional tectonics west of the Recruit Pass Fault appears to preclude significant hydrocarbon trap formation.

6. The gravity models suggest that the San Andreas Fault dips steeply in the Big Bend area even though some previous studies suggest otherwise.
7. The existence of Abel Mountain thrust in the Sawmill Mountain area is not supported by the structural models (profile A-A'). The Apache Saddle gravity model clearly indicates that the crystalline basement rocks are vertically extensive and there is no evidence for a shallow, low angle thrust fault.
8. The modern San Andreas Fault became the active trace in the Southern California at approximately 4-5 Ma. Previously San Gabriel Fault was active and the system was dominantly transtensional. Assuming that the exhumation of crystalline rocks starts with the switch from transtension to transpression, the uplift rate is 1 km/Ma. This is consistent with low temperature thermochronology studies in the Transverse Ranges.

APPENDIX A

DENSITY OF COLLECTED ROCK SAMPLES

Station name	Sample description	Dry Weight (g)	Volume 1	Volume 2	Volume 3	Density 1	Density 2	Density 3	Average density
14CA002	sandstone	99.637	40.5	41.85	42	2.46	2.38	2.37	2.40
14CA007	sandstone	20.41	8.65	9.55	9.7	2.36	2.14	2.10	2.20
14CA012	diorite	16.78	6.45	6.85	6.9	2.60	2.45	2.43	2.49
14CA016	fault gouge	68.267	33.6	36.2	37.1	2.03	1.89	1.84	1.92
14CA018	siltstone	147.006	84.45	85.5	85.85	1.74	1.72	1.71	1.72
14CA019-A	siltstone	155.273	107.2	108.8	109.3	1.45	1.43	1.42	1.43
14CA019-B	shattered siltstone	11.511	8			1.44			1.44
14CA026	siltstone	14.084	8.7	8.9	9	1.62	1.58	1.56	1.59
14CA033-A	siltstone	16.09	9.35	9.9	9.95	1.72	1.63	1.62	1.65
14CA033-B	sandstone	6.539	3.1	3.6	3.75	2.11	1.82	1.74	1.89
14CA045	sandstone	58.158	37.8	38.15	38.3	1.54	1.52	1.52	1.53
14CA062	sandstone	50.503	26.2	26.2	26.25	1.93	1.93	1.92	1.93
14CA068	diorite	8.029	3.15	3.3	3.25	2.55	2.43	2.47	2.48
14CA069-A	sandstone	121.245	50.25	51.9	52	2.41	2.34	2.33	2.36
14CA069-B	granite	52.206	20.15	20.75	21	2.59	2.52	2.49	2.53
14CA069-C	gabbro	9.72	3.85	4.2	4.2	2.52	2.31	2.31	2.38
14CA069-D	fault gouge	100.667	43.8	46.75	47.35	2.30	2.15	2.13	2.19
14CA070-A	white sandstone	13.835	5.8	6.3	6.25	2.39	2.20	2.21	2.26
14CA070-B	pink sandstone	9.122	3.6	4.3	4.3	2.53	2.12	2.12	2.26
14CA075-A	granodiorite	23.265	8.85	9.25	9.35	2.63	2.52	2.49	2.54
14CA075-B	sandstone	174.408	70.6	72.25	72.15	2.47	2.41	2.42	2.43
14CA075-C	schist	130.436	49.05	49.95	50.15	2.66	2.61	2.60	2.62
14CA085	pink granite	4.225	1.7	1.75	1.7	2.49	2.41	2.49	2.46
14CA092	gabbro	333.167	122.15	123.8	123.8	2.73	2.69	2.69	2.70

Station name	Sample description	Dry Weight (g)	Volume 1	Volume 2	Volume 3	Density 1	Density 2	Density 3	Average density
14CA096	basalt	242.602	82.95	83.95	84.25	2.92	2.89	2.88	2.90
14CA098	basalt	540.468	185.6	187.4	187	2.91	2.88	2.89	2.90
14CA105-A	diorite	9.477	3.9	4.3	4.35	2.43	2.20	2.18	2.27
14CA105-B	schist	34.416	12.8	13.85	13.85	2.69	2.48	2.48	2.55
14CA108	granodiorite	41.83	16.3	17.05	17.05	2.57	2.45	2.45	2.49
14CA110	biotite schist	64.495	24.8	26.1	26.3	2.60	2.47	2.45	2.51
14CA117	schist	35.554	13.15	13.8	13.7	2.70	2.58	2.60	2.63
14CA118	gneiss	15.908	5.65	6.05	6.1	2.82	2.63	2.61	2.68
14CA120-A	fault breccia	45.225	16.3	16.85	16.95	2.77	2.68	2.67	2.71
14CA120-B	blue schist	28.537	11.4	12.75	12.75	2.50	2.24	2.24	2.33
14CA121-A	quartz-rich schist	69.298	26.3	27.15	27.15	2.63	2.55	2.55	2.58
14CA121-B	mica-rich schist	128.748	47.45	48.45	48.35	2.71	2.66	2.66	2.68
14CA123	schist	144.801	55.45	54.3	54.95	2.61	2.67	2.64	2.64
14CA130	sandstone	25.526	10.25	10.9	10.9	2.49	2.34	2.34	2.39
14CA131	sandstone	32.816	12.9	13.6	13.8	2.54	2.41	2.38	2.44
14CA133	sandstone	164.509	66.9	68.8	68.8	2.46	2.39	2.39	2.41
14CA134	turbidites	93.25	43.55	43.4	43.3	2.14	2.15	2.15	2.15
14CA137	slate	36.792	15.4	15.9	15.85	2.39	2.31	2.32	2.34
14CA138	marble	100.235	37.3	37.95	37.85	2.69	2.64	2.65	2.66
14CA140	biotite schist	288.733	104.25	103.8	104.05	2.77	2.78	2.77	2.78
14CA143-A	granite	127.757	50	51	51.5	2.56	2.51	2.48	2.51
14CA143-B	granite	276.219	107.45	109	108.9	2.57	2.53	2.54	2.55
14CA145	granodiorite	32.599	12.7	13.5	13.5	2.57	2.41	2.41	2.47
14CA149	sandstone	203.996	84.3	84.35	84.25	2.42	2.42	2.42	2.42
14CA152	marble	100.151	38	40	40.1	2.64	2.50	2.50	2.55
14CA160	red sandstone	159.263	65.9			2.42			2.42
14CA165	conglomerate	262.104	106.6	106.5	106.7	2.46	2.46	2.46	2.46

APPENDIX B

DATA TABLE OF GRAVITY SURVEY

Station name	UTM Northing	UTM Easting	WGS 84 Latitude	WGS 84 Longitude	EGM 96 Elevation	Absolute Gravity (mgal)	Calculated Gravity (mgal)	Free-Air Anomaly	Simple Bouguer Anomaly	Interpolated Terrain Correction	Spherical Cap Correction	Complete Bouguer Anomaly
14CA001	3852023	330615.8	34.796363	-118.85154	1160.287	979402.65	979716.47	44.24491	-85.91388	6.156973	1.2209958	-80.977903
14CA002	3866404.9	279714.55	34.916207	-119.41134	1307.634	979397.71	979726.63	74.611582	-72.076314	5.110721	1.3076937	-68.273287
14CA003	3866658	279638.84	34.918471	-119.41223	1292.166	979401.13	979726.82	73.064296	-71.88843	5.062078	1.2993159	-68.125668
14CA004	3866903.5	279692.92	34.920694	-119.41171	1275.876	979405.04	979727.01	71.764777	-71.360568	5.002495	1.2903094	-67.648382
14CA005	3867122.3	279878.27	34.922705	-119.40974	1261.356	979409.37	979727.18	71.442956	-70.053563	5.161782	1.2821228	-66.173904
14CA006	3867424.9	279862.16	34.925428	-119.40999	1247.081	979412.56	979727.41	69.997029	-69.898147	4.844167	1.2739287	-66.327909
14CA007	3867738.8	279637.96	34.928207	-119.41253	1229.566	979415.58	979727.65	67.369143	-70.561234	4.552491	1.2636772	-67.27242
14CA008	3867690.7	279980.36	34.927849	-119.40877	1220.833	979418.65	979727.62	67.776717	-69.174009	4.780375	1.2584845	-65.652118
14CA009	3867791.4	280124.55	34.928787	-119.40722	1206.795	979421.96	979727.7	66.673481	-68.702489	4.780375	1.250024	-65.172138
14CA010	3868019.7	279913.76	34.930798	-119.40959	1187.638	979425.32	979727.87	63.950093	-69.27688	4.492248	1.2382529	-66.022885
14CA011	3868115.6	279620.01	34.931598	-119.41283	1173.693	979427.89	979727.94	62.152978	-69.509672	4.293684	1.2295207	-66.445509
14CA012	3868436.6	279567.06	34.934479	-119.41349	1151.031	979432.01	979728.18	59.033765	-70.086705	4.058131	1.2150356	-67.24361
14CA013	3868485.4	279900.67	34.934992	-119.40985	1136.535	979435.23	979728.23	57.740913	-69.753423	4.055769	1.205579	-66.903233
14CA014	3868326.4	280251.42	34.933635	-119.40597	1119.498	979439.72	979728.11	57.088476	-68.494682	4.197949	1.1942743	-65.491007
14CA015	3868499.3	280524.04	34.935252	-119.40304	1102.759	979442.63	979728.25	54.688989	-69.01642	4.040434	1.1829667	-66.158953
14CA016	3868740.7	280527.56	34.937427	-119.40306	1107.56	979439.26	979728.43	52.618445	-71.625531	3.937703	1.1862302	-68.874058
14CA017	3868943	280369.8	34.939216	-119.40484	1103.191	979438.8	979728.58	50.662637	-73.091232	3.876954	1.1832611	-70.397539
14CA018	3869168.2	280190.34	34.941206	-119.40686	1085.054	979441.33	979728.75	47.420247	-74.299049	3.812296	1.1707903	-71.657543
14CA019	3869338.9	280490.72	34.942809	-119.40362	1070.388	979443.07	979728.89	44.505324	-75.568767	3.866139	1.1605356	-72.863164
14CA020	3869250.7	280694.32	34.942058	-119.40137	1041.395	979450.84	979728.83	43.386628	-73.435084	3.942052	1.1398141	-70.632846
14CA021	3869523.4	280695.56	34.944515	-119.40143	1013.505	979455.55	979729.03	39.280782	-74.412283	4.014687	1.1193182	-71.516914
14CA022	3869866.4	280686.94	34.947604	-119.40161	976.525	979463.12	979729.3	35.177317	-74.367402	4.221688	1.0912912	-71.237005
14CA023	3870038.9	280413.24	34.949099	-119.40465	952.812	979467.4	979729.42	32.011685	-74.872954	4.1465	1.0728087	-71.799263

Station name	UTM Northing	UTM Easting	WGS 84 Latitude	WGS 84 Longitude	EGM 96 Elevation	Absolute Gravity (mgal)	Calculated Gravity (mgal)	Free-Air Anomaly	Simple Bouguer Anomaly	Interpolated Terrain Correction	Spherical Cap Correction	Complete Bouguer Anomaly
14CA024	3870218	280269.17	34.950681	-119.40628	941.458	979469.98	979729.56	30.956152	-74.654817	3.947455	1.0638179	-71.77118
14CA025	3870531.1	280261.35	34.9535	-119.40645	910.345	979477.35	979729.8	28.483557	-73.637214	4.070353	1.0387119	-70.605573
14CA026	3870840.8	280143.75	34.956265	-119.40781	890.738	979481.66	979730.03	26.511047	-73.410249	3.950054	1.0225377	-70.482732
14CA027	3871073.8	279994.24	34.958332	-119.40951	877.057	979484.19	979730.21	24.645655	-73.740933	4.004786	1.0110903	-70.747237
14CA028	3854581.2	327834.25	34.818953	-118.88246	1158.063	979415.13	979718.39	54.119184	-75.790122	4.196932	1.2195693	-72.812759
14CA029	3854784.4	327671.25	34.820757	-118.88428	1155.948	979416.66	979718.54	54.841346	-74.830703	4.365318	1.2182094	-71.683595
14CA030	3870951.1	280068.77	34.957243	-119.40866	883.516	979482.67	979730.11	25.212132	-73.899014	3.950054	1.0165113	-70.965471
14CA031	3871237.9	279899.21	34.95979	-119.41059	863.986	979486.48	979730.33	22.775438	-74.144869	3.880386	1.0000294	-71.264513
14CA032	3871508.7	279798.95	34.962208	-119.41176	851.454	979488.94	979730.54	21.167284	-74.347208	3.939946	0.9893107	-71.396572
14CA033	3871747	279633.93	34.964318	-119.41363	821.528	979494.69	979730.72	17.500593	-74.656857	3.837432	0.963264	-71.782689
14CA034	3872065.2	279649.71	34.967189	-119.41354	803.859	979499.14	979730.96	16.252139	-73.923236	3.834598	0.9475871	-71.036225
14CA035	3872347.4	279590.01	34.969718	-119.41427	787.4	979502.78	979731.17	14.595855	-73.73318	3.774092	0.9327845	-70.891872
14CA036	3872560	279813.46	34.971682	-119.41188	766.073	979508.47	979731.34	13.536169	-72.400444	3.81846	0.9133178	-69.495301
14CA037	3872843.9	279988.82	34.974279	-119.41004	736.711	979515.93	979731.56	11.71558	-70.92726	3.713609	0.885989	-68.09964
14CA038	3873117.5	280208.9	34.976791	-119.4077	718.051	979520.11	979731.77	9.9215835	-70.628013	3.708777	0.8683031	-67.787539
14CA039	3873305.1	280426.63	34.978528	-119.40537	706.247	979522.23	979731.92	8.2582788	-70.967167	3.687636	0.8569878	-68.136519
14CA040	3873413.7	280693.32	34.979565	-119.40248	696.894	979524.97	979732.01	8.0269327	-70.149312	3.750436	0.8479518	-67.246827
14CA041	3873636.4	280910.34	34.981619	-119.40016	680.775	979528	979732.18	5.899767	-70.468279	3.554955	0.8322333	-67.745557
14CA042	3871245.4	279893.52	34.959856	-119.41066	863.35	979487.16	979730.34	23.24877	-73.600192	3.880386	0.9994881	-70.719294
14CA043	3873296.9	280536.11	34.978479	-119.40417	703.326	979523.32	979731.92	8.4498322	-70.447942	3.687636	0.8541724	-67.614478
14CA044	3873806.2	281159.81	34.983202	-119.39747	659.787	979532.53	979732.32	3.820718	-70.192934	3.543303	0.8114906	-67.461121
14CA045	3873988.3	281472.13	34.984911	-119.3941	634.98	979537.58	979732.46	1.0673169	-70.163533	3.374986	0.7865703	-67.575117
14CA046	3874222.6	281576.72	34.987044	-119.39302	615.715	979541.3	979732.64	-1.336934	-70.406672	3.191158	0.7669161	-67.982431
14CA047	3874522.8	281658.29	34.989766	-119.3922	587.493	979546.43	979732.88	-5.1458996	-71.049748	2.884734	0.7376483	-68.902662
14CA048	3874857	281679.92	34.992782	-119.39206	584.757	979546.28	979733.13	-6.3982016	-71.99513	2.648137	0.7347809	-70.081774

Station name	UTM Northing	UTM Easting	WGS 84 Latitude	WGS 84 Longitude	EGM 96 Elevation	Absolute Gravity (mgal)	Calculated Gravity (mgal)	Free-Air Anomaly	Simple Bouguer Anomaly	Interpolated Terrain Correction	Spherical Cap Correction	Complete Bouguer Anomaly
14CA049	3875070.9	281454.9	34.99466	-119.39458	577.107	979547.3	979733.29	-7.8972851	-72.636051	2.614305	0.7267352	-70.748482
14CA050	3875323.5	281191.53	34.996888	-119.39753	563.793	979549.8	979733.48	-9.6969043	-72.942131	2.609063	0.7126334	-71.045702
14CA051	3875254.4	281264	34.996272	-119.39671	567.381	979548.88	979733.43	-9.4531292	-73.100851	2.609063	0.7164461	-71.208234
14CA052	3875432.6	281072.26	34.997836	-119.39886	557.03	979550.92	979733.56	-10.746195	-73.232761	2.702632	0.7054221	-71.235552
14CA053	3875642.2	280852.15	34.999677	-119.40132	543.632	979553.76	979733.72	-12.192912	-73.176516	2.624399	0.6910401	-71.243157
14CA054	3875850.8	280632.53	35.001509	-119.40378	530.062	979556.71	979733.87	-13.590601	-73.051949	2.630987	0.6763436	-71.097306
14CA055	3876075.5	280395.04	35.003482	-119.40644	515.493	979559.53	979734.04	-15.426743	-73.253768	2.638698	0.6604196	-71.27549
14CA056	3876267	280176.78	35.005159	-119.40888	512.483	979559.83	979734.18	-16.202703	-73.692072	2.651817	0.6571109	-71.697366
14CA057	3882573.5	281110.86	35.062181	-119.40032	257.731	979589.49	979739.03	-70.001389	-98.913163	1.616515	0.3537716	-97.650419
14CA058	3880389.6	279189.54	35.042087	-119.42079	347.125	979582.23	979737.32	-47.969396	-86.909219	2.009017	0.4654618	-85.365664
14CA059	3880180	278654.08	35.040081	-119.4266	369.403	979581.05	979737.15	-42.105568	-83.544495	2.041844	0.4924132	-81.995064
14CA060	3880064.3	278193.07	35.038937	-119.43162	384.901	979580.08	979737.05	-38.19633	-81.373793	2.191082	0.5109546	-79.693665
14CA061	3879604.5	277740.22	35.034695	-119.43646	403.192	979579.27	979736.69	-33.001558	-78.230871	2.321163	0.532618	-76.442326
14CA062	3879099.3	277334.24	35.030054	-119.44077	435.166	979576.35	979736.3	-25.651857	-74.467952	2.498565	0.5699168	-72.539304
14CA063	3878521.4	277006.39	35.024776	-119.4442	465.033	979571.42	979735.85	-20.923879	-73.090397	2.470588	0.6041022	-71.223911
14CA064	3878120.5	276616.37	35.021078	-119.44837	488.271	979567.87	979735.53	-16.98328	-71.756592	2.560165	0.6302622	-69.82669
14CA065	3877566.2	276287.21	35.016011	-119.45182	523.605	979561.48	979735.1	-12.037915	-70.774929	2.598295	0.6693047	-68.845938
14CA066	3877116.2	275895.95	35.01187	-119.45599	562.463	979553.89	979734.75	-7.2906377	-70.386668	2.692784	0.7112178	-68.405102
14CA067	3876952.8	275546.5	35.010321	-119.45977	608.294	979543.46	979734.62	-3.4389832	-71.676248	2.746956	0.7592749	-69.688567
14CA068	3877142.8	275186.2	35.011953	-119.46376	655.7	979533.23	979734.76	0.8226391	-72.732541	2.824492	0.807415	-70.715464
14CA069	3877298.9	274800.39	35.013273	-119.46803	688.498	979526.47	979734.87	4.0715404	-73.162857	2.859459	0.8397874	-71.143185
14CA070	3877461.3	274421.07	35.014651	-119.47223	725.616	979519.16	979734.99	8.1000304	-73.298193	2.715676	0.875503	-71.45802
14CA071	3877854.4	274327.91	35.018172	-119.47336	746.09	979515.27	979735.29	10.228439	-73.466519	2.59762	0.894785	-71.763684
14CA072	3878233	274287.12	35.021573	-119.47391	756.9	979513.37	979735.58	11.368002	-73.539602	2.630058	0.9048457	-71.814389
14CA073	3878559.8	274176.22	35.024493	-119.47521	745.197	979515.45	979735.83	9.597346	-73.997437	2.751822	0.8939502	-72.139565
14CA074	3878579.4	273758.74	35.024576	-119.47979	745.036	979516.85	979735.83	10.933201	-72.643521	2.327728	0.8937997	-71.209593
14CA075	3878523.1	273389.71	35.023986	-119.48381	735.301	979519.25	979735.78	10.384478	-72.10019	2.019803	0.8846612	-70.965048
14CA076	3878178.9	273071.75	35.020814	-119.4872	739.217	979517.72	979735.51	10.334818	-72.58914	1.894145	0.8883453	-71.58334

Station name	UTM Northing	UTM Easting	WGS 84 Latitude	WGS 84 Longitude	EGM 96 Elevation	Absolute Gravity (mgal)	Calculated Gravity (mgal)	Free-Air Anomaly	Simple Bouguer Anomaly	Interpolated Terrain Correction	Spherical Cap Correction	Complete Bouguer Anomaly
14CA077	3877749.8	272956.28	35.016922	-119.48835	759.902	979511.75	979735.18	11.073263	-74.171099	2.049941	0.9076249	-73.028783
14CA078	3877446.2	272977.83	35.014192	-119.48803	775.585	979508.02	979734.95	12.414411	-74.58924	2.179058	0.9220399	-73.332222
14CA079	3877020.2	273039.88	35.010368	-119.48723	795.764	979501.87	979734.63	12.822187	-76.445106	2.60372	0.9403308	-74.781717
14CA080	3876691.4	273157.06	35.007432	-119.48586	833.49	979491.59	979734.38	14.433832	-79.065492	2.633047	0.9737516	-77.406197
14CA081	3876659.4	272887.67	35.007083	-119.4888	883.083	979478.96	979734.35	17.133188	-81.929385	2.752214	1.0161489	-80.193319
14CA082	3876489.4	272632.39	35.005495	-119.49155	909.092	979473.58	979734.21	19.918218	-82.061994	2.796406	1.0376865	-80.303275
14CA083	3876288.2	272809.83	35.003722	-119.48955	903.198	979474.66	979734.06	19.330226	-81.988809	2.755793	1.0328478	-80.265864
14CA084	3875999.4	272883.55	35.001137	-119.48867	885.92	979478.72	979733.84	18.277369	-81.103453	2.553629	1.0185214	-79.568345
14CA085	3875696.5	272935.52	34.998419	-119.48802	856.033	979486.94	979733.61	17.497182	-78.530972	2.409434	0.99324	-77.114778
14CA086	3875524.8	273162.91	34.996923	-119.48548	831.196	979492.46	979733.48	15.479264	-77.762723	2.402976	0.9717482	-76.331496
14CA087	3875279.1	273073.24	34.994691	-119.48639	807.968	979498.02	979733.29	14.062679	-76.573636	2.237889	0.9512526	-75.286999
14CA088	3875154.8	272911.4	34.993534	-119.48813	805.661	979499.52	979733.2	14.951247	-75.426272	2.019504	0.9491961	-74.355964
14CA089	3875452.9	272618.76	34.996154	-119.49142	829.946	979494.4	979733.42	17.10006	-76.001704	2.146801	0.970655	-74.825558
14CA090	3875534.2	272372.5	34.996831	-119.49413	832.527	979494.4	979733.48	17.839108	-75.552189	2.016446	0.972911	-74.508654
14CA091	3875249.3	272313.52	34.994251	-119.4947	835.162	979494.5	979733.26	18.972617	-74.714268	1.740639	0.9752094	-73.948839
14CA092	3874979.1	272185.88	34.991788	-119.49603	844.319	979492.78	979733.05	20.294272	-74.419829	1.608687	0.9831583	-73.7943
14CA093	3874820.7	271924.65	34.990302	-119.49884	866.704	979487.77	979732.92	22.315117	-74.910091	1.882433	1.0023394	-74.029997
14CA094	3874564.1	271799.9	34.987962	-119.50014	892.802	979481.96	979732.72	24.752479	-75.400353	2.090903	1.0242532	-74.333703
14CA095	3874311.1	271510.99	34.985618	-119.50323	926.211	979474.55	979732.52	27.851206	-76.049383	3.493098	1.0516005	-73.607886
14CA096	3874023.9	271178.1	34.982955	-119.5068	929.639	979473.18	979732.3	27.767904	-76.517232	5.038098	1.0543617	-72.533496
14CA097	3874087.5	271019.87	34.983493	-119.50855	949.571	979468.63	979732.34	29.324128	-77.196942	5.589664	1.0702516	-72.677529
14CA098	3874029.7	270829.45	34.982929	-119.51061	940.828	979470.24	979732.3	28.285933	-77.254364	6.772296	1.0633164	-71.545384
14CA099	3873688.9	270732.73	34.979836	-119.51158	909.793	979475.92	979732.03	24.651226	-77.407623	7.537162	1.0382603	-70.908721
14CA100	3873504.3	270341.1	34.978085	-119.51581	886.632	979480.12	979731.88	21.855603	-77.60509	7.688458	1.019116	-70.935748
14CA101	3873022.3	269787.19	34.973617	-119.52174	866.868	979484.18	979731.5	20.186955	-77.05665	4.918742	1.0024786	-73.140386
14CA102	3872640.7	269030.3	34.970007	-119.52992	838.636	979489.38	979731.2	16.988467	-77.088126	2.399247	0.9782321	-75.667111
14CA103	3858794.1	303706.35	34.85255	-119.1471	1522.534	979364.66	979721.23	113.2766	-57.518366	10.80114	1.4065335	-48.12376
14CA104	3859769.1	297946.28	34.860208	-119.2103	1862.747	979298.41	979721.88	151.37165	-57.587763	10.11131	1.4960533	-48.972506

Station name	UTM Northing	UTM Easting	WGS 84 Latitude	WGS 84 Longitude	EGM 96 Elevation	Absolute Gravity (mgal)	Calculated Gravity (mgal)	Free-Air Anomaly	Simple Bouguer Anomaly	Interpolated Terrain Correction	Spherical Cap Correction	Complete Bouguer Anomaly
14CA105	3855652.3	296543.33	34.822833	-119.22464	2248.301	979196.99	979718.72	172.10194	-80.108196	16.12312	1.4983295	-65.483405
14CA106	3855747	296336.07	34.823644	-119.22693	2229.728	979201.25	979718.78	170.56376	-79.562888	15.73139	1.500635	-65.332133
14CA107	3855948.6	296154.51	34.825424	-119.22896	2210.465	979206.1	979718.94	169.31293	-78.652833	16.2865	1.5027678	-63.8691
14CA108	3856198.7	296184.13	34.827684	-119.2287	2193.627	979211.91	979719.13	169.73198	-76.344925	16.58449	1.5044168	-61.264851
14CA109	3856523.5	296205.9	34.830615	-119.22854	2169.865	979217.12	979719.38	167.36656	-76.044773	16.41164	1.5064021	-61.139535
14CA110	3856572.3	296453.3	34.831104	-119.22585	2170.343	979220.42	979719.42	170.77268	-72.692269	16.97869	1.5063661	-57.219945
14CA111	3856827.5	296567.36	34.833427	-119.22466	2152.673	979225.76	979719.61	170.4654	-71.017364	16.9984	1.507589	-55.526553
14CA112	3857012.7	296755.63	34.835133	-119.22265	2128.87	979231.87	979719.76	169.08574	-69.72685	17.59489	1.5088866	-53.640847
14CA113	3857225.5	296986.03	34.837097	-119.22018	2110.201	979237.83	979719.92	169.11673	-67.601602	18.30109	1.5096234	-50.810136
14CA114	3857238.1	297199.52	34.837253	-119.21785	2097.602	979241.39	979719.94	168.7687	-66.536305	19.93656	1.509981	-48.109726
14CA115	3857393.6	297314.35	34.838676	-119.21664	2061.909	979244.93	979720.06	161.17799				
14CA116	3857618	297053.58	34.840647	-119.21954	2057.897	979251.9	979720.23	166.74431	-64.106661	16.48763	1.5103722	-49.129403
14CA117	3857811.8	296823.83	34.842347	-119.2221	2039.859	979256.64	979720.37	165.76857	-63.058936	14.44286	1.5101808	-50.126257
14CA118	3858029	296623.86	34.844264	-119.22434	2022.474	979260.19	979720.53	163.79008	-63.087205	12.82275	1.5097782	-51.774234
14CA119	3858315.1	296579.02	34.846833	-119.2249	2007.442	979264.58	979720.75	163.32647	-61.864559	12.14364	1.5092573	-51.230176
14CA120	3858546.1	296606.03	34.848921	-119.22466	1991.041	979268.73	979720.93	162.24068	-61.110518	11.47764	1.5085064	-51.141384
14CA121	3858772	296803.65	34.850996	-119.22255	1975.743	979272.34	979721.1	160.95616	-60.678936	11.2849	1.5076341	-50.90167
14CA122	3858658.4	297009.46	34.850013	-119.22027	1960.214	979276.58	979721.02	160.48407	-59.409015	11.78229	1.5065789	-49.133304
14CA123	3858694.7	297210.56	34.85038	-119.21809	1950.656	979278.83	979721.05	159.74842	-59.072466	12.30737	1.5058445	-48.27094
14CA124	3858991	297339.52	34.853076	-119.21675	1931.842	979283.13	979721.28	158.01832	-58.692041	11.35561	1.5042097	-48.840641
14CA125	3859032.7	297612.86	34.853506	-119.21377	1916.348	979286.86	979721.32	156.93089	-58.041382	11.12341	1.5026751	-48.420647
14CA126	3859278.7	297795.24	34.855759	-119.21184	1898.873	979290.71	979721.51	155.19576	-57.816209	10.59237	1.50074	-48.724579
14CA127	3859526	297923.7	34.858013	-119.21049	1887.599	979293.27	979721.7	154.0829	-57.664367	10.16461	1.4993767	-48.999134
14CA128	3859904.6	297872.58	34.861415	-119.21114	1853.179	979299.56	979721.99	149.46874	-58.417358	10.43049	1.4946571	-49.481525
14CA129	3860007.2	297710.19	34.862306	-119.21294	1851.356	979300.34	979722.06	149.60706	-58.074542	10.12904	1.4943837	-49.439885
14CA130	3860081.5	297973.59	34.863028	-119.21008	1886.734	979292.53	979722.12	152.65651	-58.993726	11.48409	1.4992684	-49.008905
14CA131	3860252.7	298062.5	34.864589	-119.20915	1913.43	979286.76	979722.26	154.98964	-59.655303	12.51859	1.502367	-48.63908
14CA132	3860430.7	298023.17	34.866185	-119.20962	1942.094	979280.24	979722.39	157.18432	-60.676096	13.74663	1.5051317	-48.434597

Station name	UTM Northing	UTM Easting	WGS 84 Latitude	WGS 84 Longitude	EGM 96 Elevation	Absolute Gravity (mgal)	Calculated Gravity (mgal)	Free-Air Anomaly	Simple Bouguer Anomaly	Interpolated Terrain Correction	Spherical Cap Correction	Complete Bouguer Anomaly
14CA133	3860458.6	298219.2	34.866475	-119.20749	1969.926	979273.94	979722.41	159.44402	-61.538537	14.3092	1.5072588	-48.736596
14CA134	3860712.1	298336.14	34.868783	-119.20627	2004.555	979266.72	979722.61	162.71024	-62.156934	15.68506	1.509139	-47.981013
14CA135	3860899.7	298484.53	34.870503	-119.20469	2037.372	979259.69	979722.76	165.66967	-62.878847	17.6522	1.5101364	-46.736783
14CA136	3861015.7	298512.01	34.871553	-119.20442	2066.989	979252.92	979722.85	167.95154	-63.919355	18.82589	1.5103813	-46.603846
14CA137	3860982.2	298787.72	34.871306	-119.2014	2106.932	979242.2	979722.82	169.57163	-66.78	18.81137	1.509727	-49.478357
14CA138	3861106.5	299010.87	34.87247	-119.19899	2127.38	979237.15	979722.92	170.73611	-67.909335	20.59971	1.5089545	-48.818579
14CA139	3861085.3	299284.05	34.872333	-119.19599	2128.856	979237.13	979722.91	171.18631	-67.624712	21.13746	1.5088873	-47.996139
14CA140	3860886.1	299493.04	34.870579	-119.19366	2153.642	979230.89	979722.76	172.73837	-68.853091	20.19891	1.5075277	-50.161709
14CA141	3860940.4	300467.71	34.871261	-119.18302	2216.447	979213.61	979722.82	174.78556	-73.851249	23.85363	1.5021336	-51.499752
14CA142	3861024.1	301142.66	34.872147	-119.17566	2269.665	979197.22	979722.9	174.74301	-79.863699	28.68324	1.4953753	-52.675834
14CA143	3862035	297463.11	34.880529	-119.21613	2006.124	979265.76	979723.61	161.24056	-63.802619	21.62986	1.509204	-43.681963
14CA144	3861919.5	297272.52	34.879451	-119.21819	2007.729	979266.32	979723.52	162.3928	-62.83042	21.28885	1.5092688	-43.050838
14CA145	3861687.3	297096.92	34.877323	-119.22005	1972.831	979274.04	979723.33	159.51784	-61.790592	20.30745	1.5074492	-42.990592
14CA146	3861482.9	296907.69	34.875444	-119.22207	1940.391	979280.95	979723.18	156.57856	-61.090811	18.80832	1.5049837	-43.787475
14CA147	3861414.8	296926.25	34.874834	-119.22185	1906.825	979288.43	979723.12	153.74966	-60.154346	18.80832	1.5016474	-42.847674
14CA148	3861143.4	296824.77	34.872368	-119.2229	1872.801	979295.81	979722.91	150.84391	-59.243347	15.48826	1.4974505	-45.252538
14CA149	3860942.2	296737.24	34.870537	-119.2238	1842.598	979302.54	979722.76	148.40515	-58.29399	13.68978	1.4930375	-46.097248
14CA150	3860717.8	296492.08	34.868466	-119.22643	1800.773	979310.68	979722.58	143.81816	-58.189131	12.0301	1.4858586	-47.64489
14CA151	3860514.1	296393.08	34.866611	-119.22746	1790.08	979312.64	979722.43	142.63363	-58.174139	10.86067	1.4838242	-48.797294
14CA152	3860281.2	296217.81	34.864477	-119.22932	1770.768	979316.75	979722.25	140.96514	-57.676251	9.758286	1.4799445	-49.397909
14CA153	3860137.4	296323.79	34.863202	-119.22813	1751.623	979321.47	979722.14	139.88302	-56.610722	9.136209	1.4758375	-48.950351
14CA154	3860133.5	296439.21	34.863191	-119.22687	1755.132	979320.56	979722.14	140.05959	-56.827785	9.286648	1.4766097	-49.017746
14CA155	3859858.3	296281.09	34.86068	-119.22853	1724.162	979327.72	979721.92	137.87225	-55.54097	8.761263	1.4694928	-48.2492
14CA156	3859705.7	296044.62	34.859257	-119.23108	1706.265	979331.78	979721.8	136.5295	-54.876066	8.499869	1.4650701	-47.841267
14CA157	3859570.9	295844.65	34.858002	-119.23323	1687.645	979335.83	979721.7	134.94092	-54.375886	8.424818	1.4602276	-47.411296
14CA158	3859614.8	295536.21	34.858335	-119.23661	1659.665	979341.06	979721.72	131.51084	-54.667225	8.269664	1.4524888	-47.85005
14CA159	3859790.5	295379.45	34.859887	-119.23837	1640.672	979344.64	979721.86	129.09659	-54.95088	8.269664	1.4469193	-48.128136
14CA160	3859907.6	295076.21	34.860882	-119.24171	1618.135	979349.64	979721.94	127.05387	-54.465439	8.397666	1.4399788	-47.507752

Station name	UTM Northing	UTM Easting	WGS 84 Latitude	WGS 84 Longitude	EGM 96 Elevation	Absolute Gravity (mgal)	Calculated Gravity (mgal)	Free-Air Anomaly	Simple Bouguer Anomaly	Interpolated Terrain Correction	Spherical Cap Correction	Complete Bouguer Anomaly
14CA161	3859936	294793.4	34.86108	-119.24481	1586.447	979356.54	979721.96	124.16201	-53.802596	8.475667	1.429611	-46.75654
14CA162	3859961.2	294697.15	34.861287	-119.24587	1563.478	979361.22	979721.98	121.73199	-53.655996	8.605347	1.4216509	-46.4723
14CA163	3859858	294400.37	34.860298	-119.24909	1539.878	979365.81	979721.89	119.12429	-53.616301	8.776667	1.4130824	-46.252716
14CA164	3859502.1	293547.1	34.856919	-119.25833	1480.154	979376.59	979721.6	111.7578	-54.283064	8.392813	1.389634	-47.279885
14CA165	3859249.6	292675.79	34.854466	-119.26779	1431.944	979385.04	979721.4	105.545	-55.087754	6.705349	1.3688611	-49.751266
14CA166	3852023.3	330616.21	34.796365	-118.85154	1160.292	979401.91	979716.47	43.503519	-86.655832	6.156973	1.220999	-81.719858

APPENDIX C

PARAMETERS OF STRUCTURAL MODELS

C.1. Parameters of Structural Model A-A'

LeftEdge,-4000

RightEdge,8000

Bottom,7000

ProfileAzimuth,0

Latitude,40

Body,1,-0.05,0.001,6,0.0001,0,1.033414

X,-618.9376,Z,-3580.153

X,-896.0739,Z,-2030.534

X,-1219.4,Z,0

X,1321.016,Z,0

X,1182.448,Z,-7000

X,-73.903,Z,-7000

Color,52,229,22

Body,2,0.2,0.001,4,0.0001,0,1.033414

X,1330.254,Z,0

X,2337.182,Z,0

X,2069.284,Z,-7000

X,1191.686,Z,-7000

Color,22,81,229

Body,3,-0.07,0.001,7,0.0001,0,1.033414

X,2346.42,Z,0

X,2568.129,Z,0

X,3270.208,Z,0

X,3140.878,Z,-1362.595

X,3085.45,Z,-1896.947

X,2632.794,Z,-7000

X,2073.134,Z,-7000

Color,229,22,111

Body,4,-0.075,0.001,6,0.0001,0,1.033414

X,4120.092,Z,-2297.71

X,4055.427,Z,-1335.878

X,3926.097,Z,0

X,4591.224,Z,0

X,4120.092,Z,-5637.405

X,4110.854,Z,-4595.42

Color,0,0,64

Body,6,-0.05,0.001,7,0.0001,0,1.033414

X,4748.268,Z,0

X,5413.395,Z,0

X,5090.069,Z,-1335.878

X,4877.598,Z,-2137.405

X,4360.277,Z,-4595.42

X,4304.85,Z,-4782.443

X,4249.423,Z,-4996.183

Color,229,22,199

Body,7,-0.075,0.001,6,0.0001,0,1.033414

X,5408.776,Z,0

X,6143.187,Z,0

X,6632.794,Z,0

X,6521.94,Z,-721.374

X,5930.716,Z,-1175.573

X,5154.734,Z,-1148.855

Color,228,229,22

Body,8,0.1,0.001,11,0.0001,0,1.033414

X,4240.185,Z,-5049.618

X,4315.627,Z,-4835.877

X,4555.812,Z,-3793.893

X,4831.409,Z,-2377.863

X,5136.259,Z,-1175.573

X,5967.667,Z,-1229.008

X,6503.464,Z,-801.5267

X,6642.032,Z,0

X,8000,Z,0

X,8000,Z,-7000

X,4046.189,Z,-7000

Color,22,229,200

Body,9,0.12,0.001,11,0.0001,0,1.033414

X,3205.543,Z,-1683.206

X,3297.921,Z,-881.6794

X,3390.3,Z,0

X,3630.485,Z,0

X,3889.145,Z,0

X,4027.714,Z,-1416.031

X,4101.617,Z,-2377.863

X,4120.092,Z,-3125.954

X,4110.855,Z,-5744.275

X,4009.238,Z,-7000

X,2669.746,Z,-7000

Color,171,22,229

Body,11,-0.45,0.001,6,0.0001,0,1.033414

X,-4000,Z,0

X,-1247.113,Z,0

X,-775.9815,Z,-2832.061

X,-637.4134,Z,-3633.588

X,-304.8499,Z,-5583.969

X,-4000,Z,-5022.901

Color,22,229,112

Body,14,-0.4,0.001,4,0.0001,0,1.033414

X,3288.684,Z,0

X,3371.824,Z,0

X,2651.27,Z,-7000

X,3103.926,Z,-1923.664

Color,22,229,24

Body,13,0,0.001,4,0.0001,0,1.033414

X,-4000,Z,-5049.618

X,-304.8499,Z,-5610.687

X,-92.37875,Z,-7000

X,-4000,Z,-7000

Color,229,53,22

Body,14,-0.4,0.001,4,0.0001,0,1.033414

X,4628.176,Z,0

X,4720.554,Z,0

X,4018.476,Z,-7000

X,4443.418,Z,-2110.687

Color,22,229,24

C.2. Parameters of Structural Model B-B'

LeftEdge,-1000

RightEdge,9000

Bottom,5000

ProfileAzimuth,0

Latitude,40

Body,1,0.15,0.001,13,0.0001,0,1.033414

X,4900.462,Z,0

X,5227.868,Z,0

X,5234.787,Z,-591.6031

X,5289.453,Z,-5000

X,5320.785,Z,0

X,6021.324,Z,0

X,6813.703,Z,0

X,7052.348,Z,-1354.962

X,7406.467,Z,-2118.321

X,7722.094,Z,-2661.972

X,9000,Z,-2938.931

X,9000,Z,-5000

X,4434.95,Z,-5000

Color,52,229,22

Body,2,-0.15,0.001,4,0.0001,0,1.033414

X,4165.512,Z,0

X,4886.451,Z,0

X,4419.554,Z,-5000

X,4042.34,Z,-5000

Color,229,22,199

Body,3,-0.5,0.001,4,0.0001,0,1.033414

X,4026.944,Z,0

X,4150.115,Z,0

X,4034.642,Z,-5000

X,4034.642,Z,-1267.606

Color,228,229,22

Body,4,-0.15,0.001,10,0.0001,0,1.033414

X,-1000,Z,0

X,2625.866,Z,0

X,2648.961,Z,-1042.254

X,2202.463,Z,-1154.93

X,1706.005,Z,-1011.45

X,1340.262,Z,-704.2254

X,909.1609,Z,-746.4789

X,613.8221,Z,-1087.786

X,44.95766,Z,-2557.252

X,-1000,Z,-3301.527

Color,22,229,200

Body,5,0.15,0.001,11,0.0001,0,1.033414

X,-1000,Z,-3323.944

X,54.65743,Z,-2577.465

X,208.622,Z,-2183.099

X,616.6282,Z,-1112.676

X,893.7644,Z,-774.6479

X,1347.96,Z,-718.3099

X,1686.682,Z,-1014.085

X,2207.852,Z,-1183.206

X,2656.659,Z,-1070.423

X,2787.529,Z,-5000

X,-1000,Z,-5000

Color,171,22,229

Body,10,-0.5,0.001,4,0.0001,0,1.033414

X,5250.962,Z,0

X,5312.548,Z,0

X,5302.309,Z,-1469.466

X,5289.453,Z,-5000

Color,229,141,22

Body,11,-0.15,0.001,4,0.0001,0,1.033414

X,2782.91,Z,0

X,4003.849,Z,0

X,4011.547,Z,-1259.542

X,2787.529,Z,-1253.521

Color,22,229,112

Body,12,0.15,0.001,4,0.0001,0,1.033414

X,2803.695,Z,-1278.626

X,4019.246,Z,-1278.626

X,4019.246,Z,-5000

X,2833.718,Z,-5000

Color,83,22,229

Body,13,-0.4,0.001,4,0.0001,0,1.033414

X,2648.414,Z,0

X,2762.125,Z,0

X,2810.624,Z,-5000

X,2672.055,Z,-1056.338

Color,229,53,22

Body,14,-0.6,0.001,8,0.0001,0,1.033414

X,6827.945,Z,0

X,9000,Z,0

X,9000,Z,-2929.577

X,8353.349,Z,-2786.26

X,7729.792,Z,-2652.672

X,7391.07,Z,-2041.985

X,7067.744,Z,-1335.878

X,6944.573,Z,-763.3588

Color,229,141,22

C.3. Parameters of Structural Model C-C'

LeftEdge,-4000

RightEdge,11000

Bottom,5000

ProfileAzimuth,0

Latitude,40

Body,1,-0.2,0.001,8,0.0001,0,1.033414

X,-4000,Z,0

X,2131.64,Z,0

X,2073.903,Z,-2816.901

X,1288.684,Z,-3091.603

X,-50.80831,Z,-3664.122

X,-1424.942,Z,-3950.382

X,-2371.824,Z,-4141.221

X,-4000,Z,-4484.733

Color,52,229,22

Body,2,0.1,0.001,5,0.0001,0,1.033414

X,2143.187,Z,0

X,2304.85,Z,0

X,2489.607,Z,-5000

X,2189.376,Z,-3454.198

X,2073.903,Z,-2824.427

Color,22,81,229

Body,3,-0.55,0.001,4,0.0001,0,1.033414

X,2327.945,Z,0

X,2570.439,Z,0

X,2524.249,Z,-5000

X,2466.513,Z,-4312.977

Color,229,22,111

Body,4,-0.55,0.001,12,0.0001,0,1.033414

X,5549.654,Z,0

X,6704.388,Z,0

X,6715.935,Z,-400.7634

X,6300.231,Z,-1011.45

X,5942.263,Z,-1603.053

X,5399.538,Z,-1676.056

X,4937.644,Z,-1366.197

X,4602.771,Z,-954.1985

X,4602.771,Z,-820.6107

X,4602.771,Z,-629.771

X,4602.771,Z,-419.8473

X,4602.771,Z,0

Color,140,229,22

Body,5,-1,0.001,4,0.0001,0,1.033414

X,6739.03,Z,0

X,6842.956,Z,0

X,6681.293,Z,-5000

X,6681.293,Z,-3778.626

Color,22,170,229

Body,6,-0.55,0.001,12,0.0001,0,1.033414

X,6831.409,Z,-830.9859

X,6842.956,Z,0

X,7789.838,Z,0

X,8170.901,Z,-114.5038

X,8505.774,Z,-211.2676

X,10053.12,Z,-114.5038

X,10180.14,Z,0

X,11000,Z,0

X,11000,Z,-2423.664

X,10053.12,Z,-1845.07

X,8390.3,Z,-1098.592

X,7628.176,Z,-935.1145

Color,229,22,199

Body,8,0.1,0.001,12,0.0001,0,1.033414

X,4602.771,Z,-5000

X,4614.318,Z,-3830.879

X,4602.771,Z,-2748.092

X,4602.771,Z,-1812.977

X,4579.677,Z,-954.1985

X,4960.739,Z,-1412.214

X,5422.633,Z,-1718.31

X,5942.263,Z,-1622.137

X,6300.231,Z,-1011.45

X,6727.483,Z,-400.7634

X,6658.199,Z,-5000

X,5653.579,Z,-5000

Color,22,229,200

Body,9,0.1,0.001,7,0.0001,0,1.033414

X,-4000,Z,-4522.901

X,-2406.467,Z,-4179.389

X,-108.545,Z,-3702.29

X,1277.136,Z,-3129.771

X,2062.356,Z,-2845.07

X,2466.513,Z,-5000

X,-4000,Z,-5000

Color,171,22,229

Body,10,0.1,0.001,8,0.0001,0,1.033414

X,6819.861,Z,-845.0704

X,7639.723,Z,-957.7465

X,8390.3,Z,-1125.954

X,9394.919,Z,-1564.885

X,10053.12,Z,-1859.155

X,10976.91,Z,-2423.664

X,10976.91,Z,-5000

X,6681.293,Z,-5000

Color,229,141,22

Body,11,-0.75,0.001,4,0.0001,0,1.033414

X,7801.386,Z,0

X,10168.59,Z,0

X,10041.57,Z,-56.33803

X,8494.226,Z,-183.0986

Color,22,229,112

Body,12,-1,0.001,4,0.0001,0,1.033414

X,4498.845,Z,0

X,4579.677,Z,0

X,4591.224,Z,-5000

X,4510.393,Z,-1774.809

Color,83,22,229

Body,13,-0.55,0.001,6,0.0001,0,1.033414

X,2581.986,Z,0

X,3678.984,Z,0

X,3678.984,Z,-877.8626

X,3448.037,Z,-915.493

X,3159.353,Z,-1084.507

X,2570.439,Z,-1676.056

Color,229,53,22

Body,14,0.1,0.001,6,0.0001,0,1.033414

X,2558.891,Z,-1717.557

X,3136.259,Z,-1125.954

X,3436.49,Z,-957.7465

X,3678.984,Z,-916.0305

X,3690.531,Z,-5000

X,2535.797,Z,-5000

Color,22,229,24

Body,15,-1,0.001,4,0.0001,0,1.033414

X,3702.079,Z,0

X,3806.005,Z,0

X,3716.914,Z,-5000

X,3678.984,Z,-1749.046

Color,22,51,229

Body,16,-0.55,0.001,4,0.0001,0,1.033414

X,3829.099,Z,0

X,4464.203,Z,0

X,4475.751,Z,-877.8626

X,3817.552,Z,-553.4351

Color,229,22,80

Body,17,0.1,0.001,4,0.0001,0,1.033414

X,3806.005,Z,-553.4351

X,4487.298,Z,-896.9466

X,4568.129,Z,-5000

X,3725.173,Z,-5000

Color,109,229,22

C.4. Parameters of Structural Model D-D'

LeftEdge,-3000

RightEdge,15000

Bottom,5000

ProfileAzimuth,0

Latitude,40

Body,1,-0.6,0.001,11,0.0001,0,1.033414

X,7832.948,Z,0

X,9428.021,Z,0

X,12008.3,Z,-171.7557

X,14971.78,Z,-267.1756

X,14970.29,Z,-3110.687

X,14374.67,Z,-2786.26

X,13281.76,Z,-2213.74

X,11618.94,Z,-1431.298

X,10191.69,Z,-1145.038

X,8390.3,Z,-725.1908

X,7794.457,Z,-477.0992

Color,52,229,22

Body,3,-0.5,0.001,8,0.0001,0,1.033414

X,5244.804,Z,-2328.244

X,5466.513,Z,-1412.214

X,6131.64,Z,-1240.458

X,7024.634,Z,0

X,7295.227,Z,0

X,7822.171,Z,0

X,7614.319,Z,-2480.916

X,6491.917,Z,-2232.824

Color,229,22,111

Body,4,-0.6,0.001,4,0.0001,0,1.033414

X,5643.883,Z,0

X,6996.151,Z,0

X,5979.215,Z,-477.0992

X,5660.508,Z,-725.1908

Color,140,229,22

Body,5,-0.85,0.001,8,0.0001,0,1.033414

X,4842.956,Z,0

X,5314.473,Z,0

X,5619.105,Z,0

X,5632.794,Z,-706.1069

X,5660.508,Z,-782.4427

X,5452.656,Z,-1431.298

X,5217.09,Z,-2366.412

X,5054.254,Z,-5000

Color,22,170,229

Body,6,-0.6,0.001,18,0.0001,0,1.033414

X,-3000,Z,0

X,1627.021,Z,0

X,2224.018,Z,-782.4427

X,2459.584,Z,-1030.534

X,2501.155,Z,-1011.45

X,1881.18,Z,0

X,4815.242,Z,0

X,4842.956,Z,-916.0305

X,4482.679,Z,-744.2748

X,3956.12,Z,-877.8626

X,3443.418,Z,-1202.29

X,3159.584,Z,-1488.55

X,2431.871,Z,-1545.802

X,1517.321,Z,-1526.718

X,741.3395,Z,-973.2824

X,297.9215,Z,-1030.534

X,-866.0508,Z,-1603.053

X,-3000,Z,-3129.771

Color,229,22,199

Body,7,0.1,0.001,12,0.0001,0,1.033414

X,7794.457,Z,-477.0992

X,8390.3,Z,-744.2748

X,10205.54,Z,-1164.122

X,11632.79,Z,-1450.382

X,13295.61,Z,-2232.824

X,14958.43,Z,-3110.687

X,14958.43,Z,-5000

X,14550.67,Z,-5000

X,14107.25,Z,-5000

X,13220.42,Z,-5000

X,11453.81,Z,-5000

X,7406.467,Z,-5000

Color,228,229,22

Body,8,0.1,0.001,5,0.0001,0,1.033414

X,5217.09,Z,-2366.412

X,6519.63,Z,-2251.908

X,7614.319,Z,-2500

X,7392.61,Z,-5000

X,5064.665,Z,-5000

Color,22,229,200

Body,9,0.1,0.001,15,0.0001,0,1.033414

X,-3000,Z,-3148.855

X,-852.194,Z,-1622.137

X,-187.067,Z,-1297.71

X,284.0647,Z,-1049.618

X,755.1963,Z,-992.3664

X,1517.321,Z,-1545.802

X,2445.727,Z,-1564.885

X,3166.282,Z,-1526.718

X,3401.848,Z,-1259.542

X,3942.263,Z,-916.0305

X,4482.679,Z,-763.3588

X,4856.813,Z,-935.1145

X,4981.524,Z,-4179.389

X,5023.095,Z,-5000

X,-3000,Z,-5000

Color,171,22,229

Body,10,-0.85,0.001,4,0.0001,0,1.033414

X,9566.975,Z,0

X,14959.58,Z,0

X,14958.43,Z,-248.0916

X,12036.52,Z,-171.7557

Color,229,141,22

Body,11,0.15,0.001,4,0.0001,0,1.033414

X,1642.032,Z,0

X,1863.741,Z,0

X,2515.012,Z,-1068.702

X,2224.018,Z,-763.3588

Color,229,141,22

Body,12,0,0.001,5,0.0001,0,1.033414

X,5951.501,Z,-496.1832

X,7004.619,Z,0

X,6145.497,Z,-1202.29

X,5480.37,Z,-1374.046

X,5660.508,Z,-744.2748

Color,83,22,229

REFERENCES

Arrowsmith, J.R., 1995, Coupled tectonic deformation and geomorphic degradation along the San Andreas Fault system, PhD. Dissertation thesis, Stanford University, 1995.

Arrowsmith, J.R., Rhodes, D.D., Pollard, D.D., 1998, Morphologic dating of scarps formed by repeated slip events along the San Andreas Fault, Carrizo Plain, California, Journal of Geophysical Research, vol. 183, no. B5, p. 10141-10160.

Atwater, Tanya, 1970, Implications of plate tectonics for the Cenozoic tectonic evolution of western North America: Geological Society of America Bulletin, v. 81, no. 12, p. 3513- 3536.

Atwater, Tanya, and Molnar, Peter, 1973, Relative motion of the Pacific and North American plates deduced from sea-floor spreading in the Atlantic, Indian, and South Pacific Oceans, *in* Kovach, R.L., and Nur, Amos, eds., Proceedings of the conference on tectonic problems of the San Andreas fault system: Stanford, Calif., Stanford University Publications in the Geological Sciences, v. 13, p. 136-148.

Bailey, E.H., Blake, M.C., Jr., and Jones, D.L., 1970, On-land Mesozoic oceanic crust in California Coast Ranges, *in* Geological Survey research, 1970: U.S. Geological Survey Professional Paper 700-C, p. C70-C81.

Bailey, E.H., Irwin, W.P., and Jones, D.L., 1964, Franciscan and related rocks, and their significance in the geology of western California: California Division of Mines and Geology Bulletin 183, 177 p.

Blome, C.D., and Irwin, W.P., 1983, Tectonic significance of late Paleozoic to Jurassic radiolarians from the North Fork terrane, Klamath Mountains, California, *in* Stevens, C.H., ed., Pre-Jurassic rocks in western North American suspect terranes: Los Angeles, Society of Economic Paleontologists and Mineralogists, Pacific Section, p. 77-89.

Blythe, A.E., Burbank, D.W., Farley, K.A., and Fielding, E.J., 2000, Structural and topographic evolution of the central Transverse Ranges, California, from apatite fissiontrack, (U-Th)/He and digital elevation model analyses, Basin Research, vol. 12, no.2, pp. 97-114.

Burchfield, B.C., and Davis, G.A., 1981, Mojave Desert and environs, *in* Ernst, W.G., ed., The geotectonic development of California (Rubey volume 1): Englewood Cliffs, N.J., Prentice-Hall, p. 217-252.

Carter, Bruce, and Silver, L.T., 1971, Post-emplacement structural history of the San Gabriel anorthosite complex [abs.]: Geological Society of America Abstracts with Programs, v. 3, no. 2, p. 92-93.

Champion, D.E., Howell, D.G., and Gromme, C.S., 1984, Paleomagnetic and geologic data indicating 2500 km of northward displacement for the Salinian and the related terranes, California: Journal of Geophysical Research, v. 89, no. B9, p. 7736-7752.

Dibblee, T.W., Jr., Johnston, R.L., Earley, J.W., Meyer, R.F., 1987, Geology and Hydrocarbon deposits of the Santa Maria, Cuyama, Taft-McKittrick, and Edna Oil Districts, Coast Ranges,

California: Appendix. Field trip guidebook, AAPG Special Volumes, Volume SG 25: Exploration for Heavy Crude Oil and Natural Bitumen, American Association of Petroleum Geologists, Tulsa, OK, pp. 685-713.

Dickinson, W.R., 1981, Plate tectonics and the continental margin of California, *in* Ernst, W.G., ed., The geotectonic development of California (Rubey volume 1): Englewood Cliffs, N.J., Prentice-Hall, p. 1-28.

Dickinson, W.R., and Snyder, W.S., 1979, Geometry of triple junctions related to San Andreas transform: Journal of Geophysical Research, v. 84, no. B2, p. 561-572.

Ehlig, P.L., 1981, Origin and tectonic history of the basement terrane of the San Gabriel Mountains, central Transverse Ranges, *in* Ernst, W.G., ed., The geotectonic development of California (Rubey volume 1): Englewood Cliffs, N.J., Prentice-Hall, p. 253-283

Fuis, G.S., Mooney, W.D., Healey, J.H., McMechan, G.A., and Lutter, W.J., 1982, Crustal structure in the Imperial Valley region, *in* The Imperial Valley, California, earthquake of October 15, 1979: U.S. Geological Survey Professional Paper 1254, p. 25-49.

Fuis, G.S., Scheirer, D.S., Langenheim, V.E., Kohler, M.D., 2012, A new perspective on the geometry of the San Andreas Fault in southern California and its relationship to lithospheric structure, Bulletin of the Seismological Society of America, vol. 102, no. 1, pp. 236-251.

Harding, T.P., 1976, Tectonic significance and hydrocarbon trapping consequences of sequential folding synchronous with San Andreas faulting, San Joaquin Valley, California, Bulletin of the American Association of Petroleum Geologists, v. 60, p. 356-378.

Haxel, G.B., and Dillon J.T., 1978, The Pelona-Orocopia schist and Vincent-Chocolate Mountain thrust system, southern California, *in* Howell, D.G., and McDougall, K.A., eds., Mesozoic paleogeography of the western United States: Pacific Coast Paleogeography Symposium 2: Los Angeles, Society of Economic Paleontologists and Mineralogists, Pacific Section, p. 453-469.

Hopson, C.A., Beebe, W.J., Mattinson, J.M., Pessagno, E.A., Jr., and Blome, C.D., 1986, Coast Ranges ophiolite: Jurassic tectonics [abs.]: Eos (American Geophysical Union Transactions), v. 67, no. 44, p. 1232.

Hopson, C.A., Mattinson, J.M., and Pessagno, E.A., Jr., 1981, Coast Range ophiolite, western California, *in* Ernst, W.G., ed., The geotectonic development of California (Rubey volume 1): Englewood Cliffs, N.J., Prentice-Hall, 418-510.

Irwin, W.P., 1977, Ophiolitic terranes of California, Oregon, and Nevada, *in* Coleman, R.G., and Irwin, W.P., eds., North American ophiolites: Oregon Department of Geology and Mineral Industries Bulletin 95, p. 75-92.

Irwin, W.P., Jones, D.L., and Pessagno, E.A., Jr., 1977, Significance of Mesozoic radiolarians from the pre-Nevadan rocks of the southern Klamath Mountains, California: Geology, v. 5, no. 9, p. 557-562.

Kellogg, K.S., Miggins, D.P., 2002, Geologic map of the Sawmill Mountain Quadrangle, Kern and Ventura Counties, California, scale: 1/24000, USGS Open File Report, 03-153.

King, P.B., 1959, The evolution of North America: Princeton, N.J., Princeton University Press, 190 p.

Larson, R.L., Menard, H.W., and Smith, S.M., 1968, Gulf of California: A result of ocean-floor spreading and transform faulting: Science, v. 161, no. 3843, p. 781-784.

McKenzie, D.P., and Morgan, W.J., 1969, Evolution of triple junctions: Nature, v. 224, no. 5215, p. 125-133.

McLaughlin, R.J., Blake, M.C., Jr., Griscom, Andrew, Blome, C.D., and Murchey, B.L., 1988, Tectonics of formation, translation, and dispersal of the Coast Range ophiolite of California: Tectonics, v. 7, no. 5, p. 1033-1056.

Minster, J.B., and Jordan, T.H., 1978, Present-day plate motions: Journal of Geophysical Research, v. 83, no. B11, p. 5331-5354.

Niemi, N.A., Buscher, J.T., Spotila, J.A., House, M.A., and Kelley, S.A., 2013, Insights from the low-temperature thermochronometry into transpressional deformation and crustal exhumation along the San Andreas Fault in the western Transverse Ranges, California, Tectonics, vol. 32, p. 1602-1622, doi:10.1002/2013TC003377.

Page, B.M., 1981, The southern Coast Ranges, *in* Ernst, W.G., ed., The geotectonic development of California (Rubey volume 1): Englewood Cliffs, N.J., Prentice-Hall, p. 329-417.

Page, B.M., 1982, Migration of Salinian composite block, California, and disappearance of fragments: American Journal of Science, v. 282, no. 10, p. 1694-1734.

Ross, D.C., 1977, Pre-intrusive metasedimentary rocks of the Salinian Block, California – a paleotectonic dilemma, *in* Stewart, J.H., and others, eds., Paleozoic paleogeography of the western United States: Pacific Coast Paleogeography Symposium 1: Los Angeles, Society of Economic Paleontologists and Mineralogists, Pacific Section, p. 371-380.

Ross, D.C., 1978, The Salinian block: A Mesozoic granitic orphan in the California Coast Ranges, *in* Howell, D.G., and McDougall, K.A., eds., Mesozoic paleogeography of the western United States: Pacific Coast Paleogeography Symposium 2: Los Angeles, Society of Economic Paleontologists and Mineralogists, Pacific Section, p. 509-522.

Ross, D.C., 1984, Possible correlations of basement rocks across the San Andreas, San Gregorio-Hosgri, and Rinconada-Reliz-King City faults, California: U.S. Geological Survey Professional Paper 1317, 37 p.

Silver, L.T., 1966, Preliminary history for the crystalline complex of the central Transverse Ranges, Los Angeles County, California [abs.]: Geological Society of America, Annual Meeting, 79th, San Francisco, 1966, Program, p. 201-202.

Silver, L.T., 1971, Problems of crystalline rocks of the Transverse Ranges [abs.]: Geological Society of America Abstracts with Programs, v. 3, no. 2, p. 193-194.

Wallace, R.E., 1973, Surface fracture patterns along the San Andreas Fault, *in* Kovach, R.L., and Nur, Amos, eds., Proceedings of the conference on tectonic problems of the San Andreas fault

system: Stanford, Calif., Stanford University Publications in the Geological Sciences, v. 13, p. 248-250.

Wallace, R.E., ed., 1990, The San Andreas Fault system, California, U.S. Geological Survey Professional Paper 1515, 283 p.

Weldon, R.J., and Humphreys, E.D., 1986, A kinematic model of southern California: Tectonics, v. 5, no. 1, p. 33-48.

BIOGRAPHICAL SKETCH

Ali Can Altintas is currently a graduate student at the Florida State University. In December 2015, he will graduate with a Master of Science in Geology with a focus in structural geology and tectonics. He got his Bachelor's degree in Geophysical Engineering at Sakarya University, Turkey. Mr. Altintas is a member of a number of professional and student organizations including American Association of Petroleum Geologists (AAPG), Geological Society of America (GSA), American Institute of Professional Geologists (AIPG), and Florida State University Geological Society.

In the summer of 2014, he executed a field work in California for his thesis subject. This field work provided him with valuable experience and information about gravity surveys and geology. He used these information to write his thesis and publish his work in two different conferences. His first publication was in 2015 GSA Cordilleran Section Meeting in Anchorage, AK. His other publication was in 2015 GSA Annual Meeting in Baltimore, MD. He also won On To the Future travel award for the latter conference.